Research article

Novel eco-friendly and easily recoverable bismuth-based materials for capturing and removing polyphenols from water

Melissa G. Galloni [a,b], Vasilissa Nikonova [a,c], Giuseppina Cerrato [b,d], Alessia Giordana [b,d], Pavel Pleva [e], Petr Humpolicek [f,g], Ermelinda Falletta [a,b,*], Claudia L. Bianchi [a,b]

[a] Dipartimento di Chimica, Università Degli Studi di Milano, Via Golgi 19, 20133, Milano, Italy
[b] Consorzio Interuniversitario Nazionale per La Scienza e Tecnologia Dei Materiali INSTM, Via Giusti 9, 50121, Firenze, Italy
[c] Dipartimento di Architettura e Disegno Industriale, Università Degli Studi Della Campania Luigi Vanvitelli, Via S. Lorenzo 31, 81031, Aversa, CE, Italy
[d] Dipartimento di Chimica, Università Degli Studi di Torino, Via Giuria 7, 10125, Torino, Italy
[e] Department of Environmental Protection Engineering, Faculty of Technology, Tomas Bata University in Zlin 275, 76001, Vavreckova, Zlin, Czech Republic
[f] Centre of Polymer Systems, Tomas Bata University in Zlín, Tř. Tomáše Bati 5678, 760 01, Zlín, Czech Republic
[g] Department of Lipids, Surfactant and Cosmetics Technology, Faculty of Technology, Tomas Bata University in Zlín, Nám. T. G. Masaryka 5555, 760 01, Zlín, Czech Republic

ARTICLE INFO

ABSTRACT

Olive oil production is one of the most developed Europe's sectors, producing olive oil and undesirable by-products, such as olive mill wastewater (OMWW) and organic waste. OMWW, containing large amounts of compounds (mainly polyphenols, phenols, and tannins), represents a problem. In fact, polyphenols have dual nature: *i)* antioxidant beneficial properties, useful in many industrial fields, *ii)* biorefractory character making them harmful in high concentrations. If not properly treated, polyphenols can harm biodiversity, disrupt ecological balance, and degrade water quality, posing risks to both environment and human health. From a circular economy viewpoint, capturing large quantities of polyphenols to reuse and removing their residuals from water is an open challenge. This study proposes, for the first time, a new path beyond the state-of-the-art, combining adsorption and degradation technologies by novel, eco-friendly and easily recoverable bismuth-based materials to capture large amounts of two model polyphenols (gallic acid and 3,4,5-trimethoxybenzoic acid), which are difficult to remove by traditional processes, and photodegrade them under solar light. The coupled process gave rise to collect 98% polyphenols, and to rapidly and effectively photodegrade the remaining portion from water.

1. Introduction

In a world afflicted by climate changes effects, continuously growing population and drastic decrease in natural resources, the Circular Economy (CE) approach represents a valid tool for the sustainable production and consumption. CE model aims at minimizing waste and maximizing resources reuse (Watson, 2020), as well as plays an important role in achieving some of the 169 Sustainable Development Goal (SDG) targets of the United Nations (THE 17) with special focus to those related to "Clean Water and Sanitation" (SDG 6), "Affordable and Clean Energy" (SDG 7), "Responsible Consumption and Production" (SDG 12), and "Life on Land" (SDG 15).

The agri-food industry stands out as a primary player in the paradigm

shift from a linear economy to a circular one due to the large volumes of waste produced annually (Springmann et al., 2018; Hamam et al., 2021; Al-Qodah et al., 2022).

Within the numerous agricultural sectors, olive oil production (OOP) emerges as a contributor, experiencing continuous growth. In the Mediterranean Countries, OOP is an important economic activity among the agro-industrial productions. However, many other countries (*i.e.*, Argentina, Australia, and South Africa) are emerging producers due to the promotion of intensive cultivation of olive trees. It has been estimated that the quantity of olive mill wastewater (OMWW) generated from milling operations varies between 0.5 and 1.5 cubic meters *per* olives' ton (Tosti et al., 2013). Italy, Spain, and Greece are the leading world producers of olives, releasing large amounts of these effluents

every year. OMWW thus represents a severe problem for the Mediterranean basin, and it is subject to legislative constraints (Inglezakis et al., 2012; Galloni et al., 2022a). It is considered a source of environmental pollution, and it is not suitable for biological treatments because of its bio-refractory character, mainly related to the high phenolic content, thus inhibiting biodegradation. Their presence in large quantities in industrial wastewater from sources (such as olive mills, landfills, pulp mills, wineries, and tanneries) poses a hazard, negatively impacting both environment and human health (Pan et al., 2023). However, the possibility of recovering products of interest from waste and returning them to the market is the basis for developing methods to strengthen the circular economy (Haque et al., 2023).

In this regard, phenolic compounds, abundant during olive oil production, hold particular significance. Among them, polyphenols are widely present in this type of wastewater (Galloni et al., 2022a). They are primarily recognized for their antioxidant properties naturally found in plants, making them highly valuable for biomedical applications (Galloni et al., 2022a). They can be used effectively in combination with biomaterials for wound healing (Ou et al., 2021), tissue regeneration (Gao et al., 2021), bone contact applications (Riccucci et al., 2021a, 2021b), and more. Their antioxidant activity provides significant health benefits, including protection against cancer and cardiovascular diseases (Riccucci et al., 2021c). Therefore, the ability to selectively capture them from OMWW is a significant challenge. Although they offer positive contributions to biodiversity and ecosystems due to their antioxidant properties and health benefits (Ndwabu et al., 2023), high concentrations in wastewater can harm aquatic life and disrupt ecosystems, leading to biodiversity loss, ecological imbalances, and degraded water quality (Pan et al., 2023). The substantial accumulation of these substances in production waste, coupled with the challenges in removing them, has become a pressing concern, attracting the global scientific attention (Jamrah et al., 2023). Therefore, the development of efficient and sustainable strategies aimed at capturing most of the polyphenols present in wastewater and removing the remaining traces to reach the permitted levels before discharging the water into the environment represents the emerging critical point for the research community.

On one hand, the adsorption approach is a simple and flexible technology to capture polyphenols from wastewater based on the interactions between an adsorbent and the targeted molecules to adsorb (Perez-Larran et al., 2018). So far, resins, (Buran et al., 2014; Li et al., 2011) polymers, (Saleh et al., 2008), membranes (Li et al., 2024; Yin et al., 2023), as well as activated carbon and natural adsorbents (Ena et al., 2012; Abid et al., 2022) have been largely studied and commercialized.

On the other hand, alternative processes have been developed to remove phenolic compounds from waters (*i.e.*, electrochemical oxidation, redox reactions, membrane separation, and photocatalytic degradation) (Galloni et al., 2022; Jamrah et al., 2023). In this framework, photocatalysis and particularly advanced oxidation processes (AOPs) emerged for their efficiency, high sustainability, and potential for integration into water purification systems (Djellabi et al., 2021; Galloni et al., 2024a; Melchionna and Fornasiero, 2020; Malik et al., 2023; Cordeiro et al., 2024). They can reduce polyphenols concentration, reaching high mineralization levels, thus being able to reintroduce clean water into the environment (Melchiors and Bentes Freire, 2023). In this regard, numerous photocatalytic formulations have been largely studied. Titania-containing photocatalysts have found success since 1993 due to their wide availability, chemical stability, low cost, wide bandgap values (3.2 eV for anatase and 3.0 for rutile), explaining good activity in the ultraviolet region (Galloni et al., 2022a; Rengifo-Herrera and Pulgarin, 2023; Sakthivel et al., 2003; Chen et al., 2023; Meroni et al., 2023). Zinc oxide has also emerged as an alternative photocatalyst candidate as demonstrated by the numerous papers reporting its efficiency in the photodegradation of organic pollutants, such as dyes, but also phenols, in water matrices under UV light irradiation (Sakthivel et al., 2003; Vaiano et al., 2018).

However, the wide band gap of these materials limits their applications for the cheap and more sustainable treatment processes exploiting solar light instead of the expensive UV light.

In this regard, in the last decades, a novel class of layered materials has arisen: bismuth oxyhalides (BiOX, where X is Cl, Br, or I) (Bhachu et al., 2016; Sharma et al., 2019). They are characterized by unique features, *i.e.*, high chemical and optical stability, non-toxicity, low cost, corrosion resistance, good visible light absorption (Hussain et al., 2022; Liu et al., 2023). Among the different BiOX, bismuth oxybromide (BiOBr) has gained ever more interest by the research community. In fact, compared to the other BiOX (*i.e.*, bismuth oxychloride, BiOCl, and bismuth oxyiodide, BiOI), BiOBr results a preferred choice in specific applications. It possesses a bandgap value narrower than BiOCl (*ca.* 2.6 *vs.* 3.2 eV). Moreover, even though BiOBr has a wider bandgap than BiOI (*ca.* 2.6 *vs.* 1.8 eV), it prevents electron-hole recombination, enhancing its photocatalytic performances and making it preferred to BiOI also in terms of environmental impact due to the potential toxicity of iodide (Vinoth et al., 2022). Based on these premises, BiOBr has demonstrated efficient decomposition capacity of several organic pollutants to non-toxic compounds in the environmental remediation field (Hussain et al., 2022; Cao et al., 2019).

So far, all these photocatalytic materials have been employed in the form of micro- or nano-powder, posing a significant challenge in terms of their separation and recovery from the reaction mixture for subsequent reuse. This point represents a notable drawback that cannot be ignored, particularly in the view of the industrial application (Galloni et al., 2022b, 2024b; Ma et al., 2021a, 2021b). Indeed, the recovery costs can potentially render the technology economically unfeasible and traces of photocatalyst remaining in the purified water can fail the effectiveness of the entire process (Pozzo et al., 1997). In this context, the introduction of magnetic and/or floating features in the adsorbents and photocatalytic materials can be considered an interesting solution, giving the possibility to maintain promising samples' performances, as well as easy separation from the reaction medium. In this scenario, several studies have underlined the potential of conventional titania- and zinc oxide-magnetic materials for degrading phenolic compounds present in waters (Lendzion-Bielun et al., 2020; Chang and Tseng, 2013; Feng et al., 2014; Nikazar et al., 2014), and other materials' formulation, spanning from magnetic mesoporous resorcinol–melamine–formaldehyde resins to magnesium doped binary ferrites, have been also largely explored as potential candidates for efficiently remove different phenols from waters (Heydaripour et al., 2019; Mustafa *et al.*, 2023). However, all of them suffer from some practical limitations (such as scalability, economic feasibility) that cannot be ignored and remain hot topics to investigate. In this scenario, so far, the use of BiOBr as active phase in magnetically recoverable photocatalysts has been limited for degrading herbicides and dyes (Cao et al., 2019; Li et al., 2017, 2018), and not yet investigated for removing phenols. Based on these premises, new approaches are currently explored by the research community to rationally design efficient adsorbents/photocatalysts capable of addressing the emerging challenges in energy, economy, and environmental sustainability of industrial processes (Thamarai et al., 2024). An eco-friendly effective adsorbent/photocatalyst should possess precise key attributes: it should be efficient, exhibiting good stability and durability along with regeneration capability. In addition, it should be easy to handle and manage throughout its lifecycle, non-toxic, and biocompatible (Hassaan et al., 2023). Eventually, following its use, it should be easily recoverable, and at the end of its life, it should be discarded without adverse effects on both environment and human health.

In this context, alginate is a biopolymer commonly extracted from marine sources (*e.g.*, marine algae) (Ayed et al., 2023; Faidi et al., 2022) consisting of α-(1 → 4)-linked l-guluronic acid (G) and β-(1 → 4)-linked d-mannuronic acid (M) units with different G:M ratios (Zhou et al., 2023; Askarieh et al., 2022). The (G) unit has better affinity to calcium

ions than (M) unit that is the core of the egg-box phenomenon (Li et al., 2014; Atthanaphanit et al., 2010). In addition, the carboxylate functional groups present in the alginate matrix can effectively bind other elements/substances, producing interesting alginate-based materials exploitable for different applications. This natural material has been widely used as support for encapsulating drugs (Mandal and Kundu, 2009), proteins (Somo et al., 2017) and enzymes (Nithya et al., 2018; Won et al., 2005), and it has gained attention in the water remediation field due to its non-toxicity, bioavailability, biocompatibility, low cost, promising adsorptive performances towards contaminants and easily recoverable feature (Idris et al., 2012; Peramune et al., 2022). It can be easily modified to produce highly efficient adsorbent materials for heavy metals (Gao et al., 2020) and dyes (Alver et al., 2020; Li et al., 2013; Benettayeb et al., 2022; Abakar and Khan, 2024). As representative examples, Lai and coworkers demonstrated that Ca-alginate beads properly modified with orange or banana peel cellulose are able to efficiently depollute waters containing heavy metal ions (*i.e.*, Cu^{2+}, Zn^{2+}, Pb^{2+}) (Lai et al., 2009), whereas Bee's research group developed a magnetically recoverable adsorbent made of alginate able to efficiently capture methylene blue and methyl orange under different conditions (Rocher et al., 2008).

At the same time, alginate can be used as floating support to easily immobilize photocatalysts under safe and mild conditions too. Up to now, different papers discussed the development of easily recoverable photoactive materials, but they are limited to the abatement of dyes, drug, *etc*. By way of example, Falletta et al. recently explored the potentialities of alginate beads combined with graphitic carbon nitride in the photodegradation of organic pollutants under solar light: good performances were obtained together with the easy recoverability of samples after use (Falletta et al., 2022). In this perspective, Ayed et al. (2023) have recently developed easily recoverable materials consisting of magnetic Fe_3O_4-natural iron ore/calcium alginate beads for novacron blue dye degradation in water by (photo)Fenton process: *ca.* 80% pollutant abatement was reached within 120 min, as well as good reusability without any catalyst loss.

In this framework, in the present research, we pave a new path beyond the current state-of-the-art, combining technologies and materials for effectively abating polyphenols from water matrix. We investigate for the first-time the role of bismuth immobilized in innovative materials for capturing large amounts of polyphenols and/or degrading them in aqueous solution when present in traces. Due to the novel approach proposed, different easily recoverable Bi-modified materials were developed and preliminarily tested for the capture and/or solar light photodegradation of two model polyphenols, *i.e.*, gallic acid (GA) and 3,4,5-trimethoxybenzoic acid (3,4,5-TMBA), selected for their hard removal from water. In addition, their antibacterial activity against *Escherichia coli*, *Staphylococcus aureus*, *Listeria ivanovii*, *Candida albicans*, and *Aspergillus niger* was also explored and discussed.

2. Materials and methods

2.1. Materials

Bismuth(III) nitrate pentahydrate ($Bi(NO_3)_3 \cdot 5H_2O$), glacial acetic acid (CH_3COOH), calcium bromide ($CaBr_2 \cdot 2H_2O$), alginic acid sodium salt (($OH_4C_5OCOO^- Na^+$)$_n$), iron(II) chloride tetrahydrate ($FeCl_2 \cdot 4H_2O$), iron(III) chloride hexahydrate ($FeCl_3 \cdot 6H_2O$), polyethylene glycol (PEG) 200, ammonium hydroxide solution (NH_4OH, 28–30%), gallic acid, ($C_6H_2(OH)_3CO_2H$), 3,4,5-trimethoxybenzoic acid (($CH_3O)_3C_6H_2CO_2H$) were of analytical grade and supplied from Merck. Ultra-pure water was obtained by Milli-Q® ultra-pure water system from Merck Millipore.

For the materials characterization and analyses liquid nitrogen (N_2, >99.0%, Sapio), barium sulphate ($BaSO_4$, >99.0%, Nacalai Tescue), nitric acid (HNO_3, 65.0%, Carlo Erba), hydrochloric acid (HCl, 37%, Merck), sodium hydroxide (NaOH, >99%, Carlo Erba). sodium nitrate ($NaNO_3$, >99%, Merck) acetonitrile (CH_3CN, HPLC grade, Carlo Erba),

water (H_2O, HPLC grade, Carlo Erba), formic acid (HCOOH, 98%, Merck), sodium carbonate (99.9%, Merck), sodium bicarbonate (99.9%, Merck), potassium hydrogen phthalate (99.95%, Merck) were used.

2.2. Materials preparation

2.2.1. Bismuth oxybromide (BiOBr)

BiOBr was prepared by co-precipitation method. To prepare *ca.* 1 g product, 55 mL $Bi(NO_3)_3 \cdot 5H_2O$ (5.47 mmol) 0.1 M in 10 wt% CH_3COOH aqueous solution was added dropwise to 33 mL KBr (3.28 mmol) 0.1 M aqueous solution. During the addition, a white solid was formed. The suspension was kept reacting overnight at room temperature under stirring (250 rpm). Then, the precipitate was successively recovered by filtration, washed several times with deionized water until neutral pH and dried overnight (120 °C).

2.2.2. Magnetite (Fe_3O_4)

Fe_3O_4 nanoparticles (NPs) were prepared optimizing the procedure developed by Della Pina et al. (2012). In a typical preparation, 0.3 g $FeCl_2 \cdot 4H_2O$ (1.4 mmol) and 0.8 g $FeCl_3 \cdot 6H_2O$ (2.9 mmol) were dissolved in 500 mL deionized water. 5 mL polyethylene glycol (PEG) was then added. As next step, a proper amount of ammonium hydroxide solution was added until pH equal to 10. The obtained suspension was kept reacting for 4 h at 50 °C. Successively, the obtained magnetic powder was kept at the bottom of the flask with the help of a magnet, the supernatant was removed, and the solid was washed several times with water until neutral pH and dried overnight at the air.

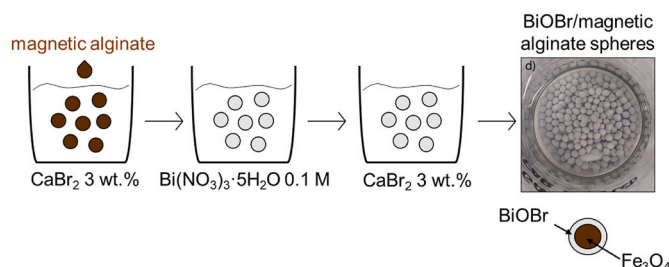#### 2.2.3. Alginates spheres and magnetic alginates spheres

Alginate spheres were prepared as recently reported by Falletta et al. (2022). In a typical preparation, 0.300 g sodium alginate was dissolved in 10 mL deionized water. The as-obtained solution was dropwise added to 50 mL $CaBr_2$ 3 wt% aqueous solution for 2 h. During the addition, the formation of alginate spheres was observed (Figure S1a). These latter were subsequently recovered and washed with water.

Magnetic alginate spheres were prepared according to the above-described procedure: 0.100 g Fe_3O_4 was added to the sodium alginate solution before the addition of $CaBr_2$ 3 wt% aqueous solution. In both cases, the as-obtained spheres were stored in deionized water (Figure S1b).

2.2.4. Bi-modified spheres

2.2.4.1. Bi^{3+}-modified alginate spheres. Bi^{3+}-modified alginate spheres were fabricated using the same procedure used for the preparation of alginate spheres, but substituting $CaBr_2$ with $Bi(NO_3)_3 \cdot 5H_2O$ as source of metal ions.

2.2.4.2. BiOBr/magnetic alginate spheres. BiOBr/magnetic alginate spheres were prepared through the following procedure (Scheme 1). The magnetic alginate spheres prepared as reported above (section 2.2.3) were immersed in: *i)* 50 mL $CaBr_2$ 3 wt% aqueous solution for 2 h, *ii)* 50 mL $Bi(NO_3)_3 \cdot 5H_2O$ 0.1 M in 10 wt% acetic acid aqueous solution for 2 h,

Scheme 1. Preparation of BiOBr/magnetic alginate spheres.

and *iii)* 50 mL CaBr$_2$ 3 wt% aqueous solution for 2 h, and washed with deionized water. This final passage in CaBr$_2$ ensured that a stable thin BiOBr layer growth onto the alginate spheres was formed. The as-obtained BiOBr/magnetic alginate spheres were stored in deionized water before the use and their feature of easily recoverability was checked with the use of a magnet (Video 1).

2.3. Characterisation

The Bi^{3+} amount into the alginate spheres was determined by Inductively Coupled Plasma Optical Emission Spectroscopy (ICP-OES) analyses on digested solids (about 50 mg sample treated with concentrated HNO$_3$ at 250 °C for 15 min) using an « Activa», Jobin Yvon ICP-OES instrument after sample drying at 50 °C for 4 h.

The BiOBr and Fe$_3$O$_4$ loadings in the BiOBr/magnetic alginate spheres were determined by atomic absorption spectroscopy (AAS) using a PinAAcle 900T instrument (S/N PTDS11062202, PerkinElmer, Waltham, MA, USA) after sample drying at 50 °C for 4 h and subsequent mineralization with nitric acid at 60 °C.

Crystal structure and phase composition were determined by X-ray powder diffraction (XRPD) using a PANanalytical X'Pert PRO diffractometer (Cu Kα = 1.54060 Å) equipped with an X-ray source operating at 40 kV × 40 mA. Diffractograms were collected in 10–80° (2θ) range with the step of 0.02° 2θ (or 0.05° 2 θ), and the time *per* each step in 5–96 s interval. Before any analyses, powder samples were finely ground and spread on an aluminium flat-plate horizontal sample holder. Patterns were identified by comparison with the JCPDS files from International Center for Diffraction Data Powder Diffraction.

Raman spectrum of BiOBr was obtained with a Bruker Vertex 70 spectrophotometer equipped with the RAMII accessory and Ge detector by exciting samples with Nd:YAG laser source (1064 nm), with resolution of 4 cm^{-1}.

Attenuated total reflection Fourier-transform infrared spectroscopy (ATR FT-IR) spectra were collected through a Bruker Vertex 70 spectrometer equipped with ATR Platinum (resolution 4 cm^{-1}). Prior to the analysis, the alginate-based materials were dried at 50 °C overnight.

Specific surface area (SSA) was determined through N$_2$ adsorption/desorption isotherms at −196 °C by an automatic analyser (Micromeritics Tristar II 3020). Before the analysis, about 1 g dried sample in powder form was outgassed at 150 °C for 4 h under vacuum to remove water and/or other volatile organic compounds adsorbed on the surface. SSA was calculated by Brunauer-Emmet-Teller (BET) equation (2-parameters, 0.05 < p/p° < 0.3, cross-sectional area of *ca.* 16.2 Å/molecule$_{N2}$).

The chemical composition of BiOBr in powder was determined by X-ray photoelectron spectroscopy (PHI 5000 Versaprobe II, ULVAC-PHI, Inc., Kanagawa, Japan) using an X-ray source (Al–Ka radiation line). The take-off angle was set at 45° for detecting photoelectrons to a depth of 1–5 nm from the surface. The binding energy of the obtained spectra was calibrated using the C1s peak (at 284.6 eV) as the reference.

Images by optical microscopy (OM) of the surfaces of the alginate-based materials were collected using a Zeiss optical microscope.

Morphology and elemental analyses were studied by a scanning electron microscope (SEM), operating with a Field Emission source (model TESCAN S9000G, Overcoached, Germany) with a source of Schottky type FEG, resolution: 0.7 nm at 15 keV (in In-Beam SE mode) and equipped with EDS Oxford Ultim Max (operated with Aztec software 6.0). Samples were supported on metallic stabs with C tape, then coated with Cr by means of ion-sputtering technique to better the material conductivity.

High resolution transmission electron images were obtained by a JEOL UHR 3010 microscope (300 kV, LaB$_6$ filament). Samples were dry dispersed onto Cu grids coated with "holey" pyrolytic carbon.

Transmission electron microscopy on Fe$_3$O$_4$ NPs was carried out by FEI Tecnai G2 F20 instrument.

The point of zero charge was determined according to the procedure previously reported in the literature (Galloni et al., 2022c). C*a.* 50 mg sample powder was added to different NaNO$_3$ solutions (20 mL, 0.1 M) under stirring. The initial pH value (pH$_{initial}$) of each NaNO$_3$ solution was adjusted in the 4.00–10.00 interval, adding 0.1 M HNO$_3$ or NaOH. The suspensions were maintained under stirring (250 rpm) for 24 h, and successively, the final pH values (pH$_{final}$) were measured after suspension centrifuge (3000 rpm for 6 min). By plotting the difference between the pH$_{final}$ and pH$_{initial}$ (ΔpH) along with the pH$_{initial}$, pH$_{pzc}$ was determined as the intersection of the resulting line at which ΔpH = 0.

The optical properties of the materials were investigated by UV–vis Diffuse Reflectance (UV-DR) spectroscopy. The optical spectra were collected at room temperature in 200–800 nm interval through a double-beam UV–Vis–NIR scanning spectrophotometer (PerkinElmer Lambda 750s UV–vis spectrophotometer, PerkinElmer, Waltham, MA, USA) equipped with an integrating sphere assembly. The as-prepared BiOBr in powder was analysed without any modification, whereas the BiOBr/magnetic alginate spheres were previously dried at 50 °C overnight and crushed to obtain a powder. The above-mentioned samples were then finely ground, uniformly pressed in a circular disk (E.D., *ca.* 4 cm), and included in the sample holder. This latter was inserted in a special quartz cuvette and placed on the window of the integrating sphere for reflectance measurements. Spectra were measured using BaSO$_4$ as the reference. The measured reflectance values (R%) were converted to absorbance (Abs, a.u.) by the equation: Abs = Log (1/R/100). To calculate the bandgap value, Tauc plot was then built according to the equation:

$$\alpha h\nu = A\left(h\nu - E_g\right)^{n/2}$$

where α is the absorption coefficient, $h\nu$ is incident photon energy, A is constant and E_g is the energy of the bandgap.

Mass loss of the alginate-based materials was determined by thermogravimetric analyses through a TGA 7, Mettler Toledo analyser. Prior to the analysis, samples were dried at 50 °C overnight and a weighed amount (*ca.* 5 mg) was loaded on the thermobalance pan. Each experiment was carried out under nitrogen flow (30 mL min^{-1}) according to the following method: *i)* heating from 30 to 800 °C at 15 °C·min^{-1}, *ii)* isothermal step at 800 °C for 5 min, and *iii)* cooling to 40 °C. In any case, the calibration of temperature was performed by measuring the Curie transitions (T$_C$) of high-purity reference materials (alumel, nickel, perkalloy, and iron: T$_C$ of 163, 354, 596, and 780 °C, respectively) at the same heating rate (β) employed for the analyses.

2.4. Adsorption and photodegradation tests

Gallic acid (GA) and 3,4,5-trimethoxybenzoic acid (3,4,5-TMBA) were selected as model polyphenols: their capture by adsorption and/or photocatalytic degradation were monitored in the dark and under solar light.

Photocatalytic degradation tests were performed under atmospheric conditions in a 250 mL batch glass cylindric reactor. The mixture, composed by the chosen photocatalytic material and the pollutant into the solution, was kept under stirring (250 rpm). The reactor was inserted in a home-made box with dark walls made of cloth. A solar lamp (ULTRA VITALUX 300W-OSRAM, power density of irradiation of 35 W m^{-2}) was installed above the reactor at the fixed height of 25 cm and kept constant throughout the experiments. These latter were performed by stirring the proper amount of the chosen photocatalyst in the reactor filled with 100 mL solution containing the single polyphenol in ultrapure water (UW) and maintained at spontaneous pH (about 5 for GA, and 5.2 for 3,4,5-TMBA). The set-up was kept in the dark for 30 min, and successively irradiated for 180 min by the solar light lamp. Polyphenols abatement was monitored for a total of 210 min, sampling 2 mL aliquots every 15 min for the first 30 min and then every 30 min for the remaining 180 min. If the chosen catalyst was in powder form, the aliquots were placed in 1.5 mL conical vials and centrifuged with a LaboGene ScanSpeed

centrifuge at 13,500 rpm for 5 min before any analyses. The collected aliquots were quantitatively analysed by HPLC-UV instrument. The HPLC instrument (Agilent 1100 Series) was equipped with a C18 Supelco column (25 cm × 4 mm, 5 μm), a 20 μL injection loop, and a UV–vis detector. Chromatographic analyses were performed by an isocratic elution of the proper mobile phase depending on the pollutant. For GA the used mobile phase was composed of 94.5% water, 5% acetonitrile and 0.5% formic acid, whereas for 3,4,5-TMBA it was composed of 69.5% water, 30% acetonitrile and 0.5% formic acid. In all cases, 0.7 mL min^{-1} flow rate was used. Pollutant abatement was monitored at 260 nm and calculated according to the following equation:

$$Pollutant\ abatement\ (\%) = \frac{C_0 - C_t}{C_0} \cdot 100\%$$

where C_0 is the initial polyphenol concentration, and C_t is the polyphenol concentration at the time t.

At the end of each abatement test, the pH values of the treated solutions were unchanged compared to the initial ones, independently of the studied polyphenols.

The effects of polyphenols concentration (10–100 ppm range) in UW and catalyst dosage (from 0.125 to 0.500 g L^{-1} for powders and from 5 to 100 g L^{-1} for spheres) were investigated.

The adsorption tests were performed as described above for the abatement ones, but in this case the system was kept under dark during the entire test time. The collected aliquots, previously diluted, were quantitatively analysed by T60 UV–visible spectrophotometer from PG Instruments at 260 nm.

All experiments were repeated three times to ensure reproducibility: a percent relative uncertainty of less than 5% was obtained.

At the end of each photocatalytic test using powder samples, the suspensions were centrifuged by a Hettich Zentrifugen D-78532 Tuttlingen centrifuge at 3000 rpm for 5 min to remove the catalyst powder and total organic carbon (TOC) analyses were performed on the supernatant. TOC analyses were performed by a Shimadzu TOC-L analyser to verify the mineralization capacity of the photocatalyst. TOC removal was evaluated by the following equation:

$$Mineralization\ capacity\ (\%) = \frac{TOC_0 - TOC_f}{TOC_0} \cdot 100\%$$

where TOC_0 is the initial TOC concentration, and TOC_f is the final one after 180 min irradiation.

2.5. Coupled experiments for polyphenols' adsorption-photodegradation

To maximize the capturing of GA (selected as model molecule for polyphenols) and successively photodegrading the remaining traces in solution, starting solutions of 500 and 1000 mg L^{-1} GA were used in these experiments. Each experiment consisted of a first adsorption test of 210 min using the Bi^{3+}-modified alginate spheres (100 g L^{-1}) to reach the high adsorption capacity of the selected pollutant, and a subsequent photodegradation test using BiOBr/magnetic alginates spheres (100 g L^{-1}) to degrade the residual polyphenol from the previous step.

2.6. Antibacterial activity

The antibacterial activity of the synthesized materials was tested against Gram-negative, Gram-positive bacteria, yeasts and molds (*Escherichia coli*, *Staphylococcus aureus*, *Listeria ivanovii*, *Candida albicans*, and *Aspergillus niger*) using the agar disk diffusion method. Samples were homogenized (Bead Mill Homogenizer, Omni international, Bead ruptor elite, SOWER, Shanghai) and due to their high viscous consistency, 250 mg each sample was used to form discs with a diameter of 6 mm. The discs were placed on agar plates previously inoculated with 1 mL 0.5 McF turbid suspension of microorganism in sterile saline solution. The antibacterial tests were also performed with pure active substances disk

(BiOBr powder was pressed). The inhibition zones around the samples were measured in mm as diameter including the disc. All tests were repeated ten times to ensure reproducibility.

3. Results and discussion

In real applications the use of traditional powders as both adsorbents and/or photocatalysts is hindered by the challenging separation and recovery from the reaction mixture for a sustainable reuse (Ma et al., 2021b; Galloni et al., 2022a). The cost associated to the recovery could render a technology economically unfeasible (Zhu et al., 2016). Moreover, traces of powders, especially if nano-sized, might possibly contaminate the environment, as they are difficult to manage and prone to dispersion. Additionally, they run the danger of invading ecosystems, or posing a threat to respiratory health, if becoming airborne and functioning as a secondary pollutant.

Considering the sustainability constraints, the immobilization strikes a compromise between the benefits of the adsorbents/photocatalysts and the need to assure their appropriate application by improving stability and facilitating simpler handling. This approach has been revealed promising as it preserves the adsorbent/photocatalytic performances, as well as it simplifies the separation from the reaction medium (Galloni et al., 2022b, 2024a; Falletta et al., 2022).

In this study, novel recoverable materials based on properly modified alginate spheres are proposed for the first time with the ambitious purpose of capturing polyphenols and/or degrading them when present in traces. Being an eco-friendly support, alginate has been selected as an inert matrix composed of numerous carboxylate functional groups that can be exploited to easily bind elements/substances with adsorptive/ photocatalytic properties, as well as bismuth sites (Wang et al., 2019a, b). So, two different Bi-alginate systems were engineered (BiOBr/alginate spheres and Bi^{3+}-modified alginate spheres, respectively), properly exploiting the surface functional groups of alginate. Then, the bismuth centres represent advantageous and available sites for the coordination of polyphenols that are characterized by the presence of several hydroxyl groups (Figure S2) (Hider et al., 2001).

Therefore, at the beginning, the chelation capability of the Ca^{2+} sites present in the bare alginate spheres was investigated to compare their chelation capability with that of the Bi-centres. Based on the obtained results, the alginate spheres' surface was then properly modified to expose Bi-centres, either as Bi^{3+} or BiOBr, and the chelation capability of Bi^{3+} centres, as well as the photocatalytic features of BiOBr, when immobilized on the surface of alginate beads, were explored. It was observed that the novel Bi^{3+}-modified alginate ensured a surface rich in positive cationic species (Bi^{3+} ions) able to promote polyphenols adsorption through a high chelation effect. Finally, the immobilization of BiOBr photocatalysts on the alginate spheres led to innovative photocatalytic composites active in the polyphenols' degradation under solar light. In this case, instead of the conventional approach of synthesizing BiOBr by co-precipitation of the Bi-precursor solution (Bi (NO$_3$)$_3$·5H$_2$O) and KBr as Br-source, an optimized procedure was proposed replacing KBr with CaBr$_2$. This ensured the production of a more stable thin BiOBr layer growing onto the alginate spheres without any BiOBr losses after washing. BiOBr in powder form was also prepared from the same precursors, characterized, and tested in the adsorption/ photodegradation of the two selected model polyphenols (GA and 3,4,5-TMBA) as the reference material. The main results obtained are critically discussed below.

3.1. Samples characterization

3.1.1. BiOBr powder

As preliminary step, BiOBr powder was synthesized as described above (starting from a CaBr$_2$ source) and properly characterized through selected physico-chemical techniques.

An insight into its crystalline structure was gained by XRPD. The

collected diffractogram (Fig. 1a) shows well defined peaks at 10.8, 21.8, 25.2, 31.7, 32.2, 39.3, 46.3, 50.7, 53.4, 57.2 and 76.8°, indexed to the (001), (002), (101), (102), (110), (112), (200), (104), (211), (212) and (310) planes of the tetragonal BiOBr phase (JCPDS 01-078-0348), demonstrating the high crystallinity of the as-obtained material (Falletta et al., 2023).

The Raman spectrum (Fig. 1b) shows the typical pattern of the tetragonal BiOBr (space group P4/*nmm*) with six signals at 60, 90, 113,

160, 385 and 425 cm^{-1} (Davies, 1973). There is only a signal in ATR-FTIR spectrum at 507 cm^{-1} attributable to the highest A_{2u} mode (Davies, 1973).

Surface chemical composition of BiOBr was investigated by XPS. The obtained results, in terms of survey and high-resolution (HR) spectra of the main detected elements, are reported in Fig. 1c–e and Figure S3. The survey spectrum (Figure S3a) reveals that the main elements present on the material's surface are Bi, O, Br, and C, with detected compositions of
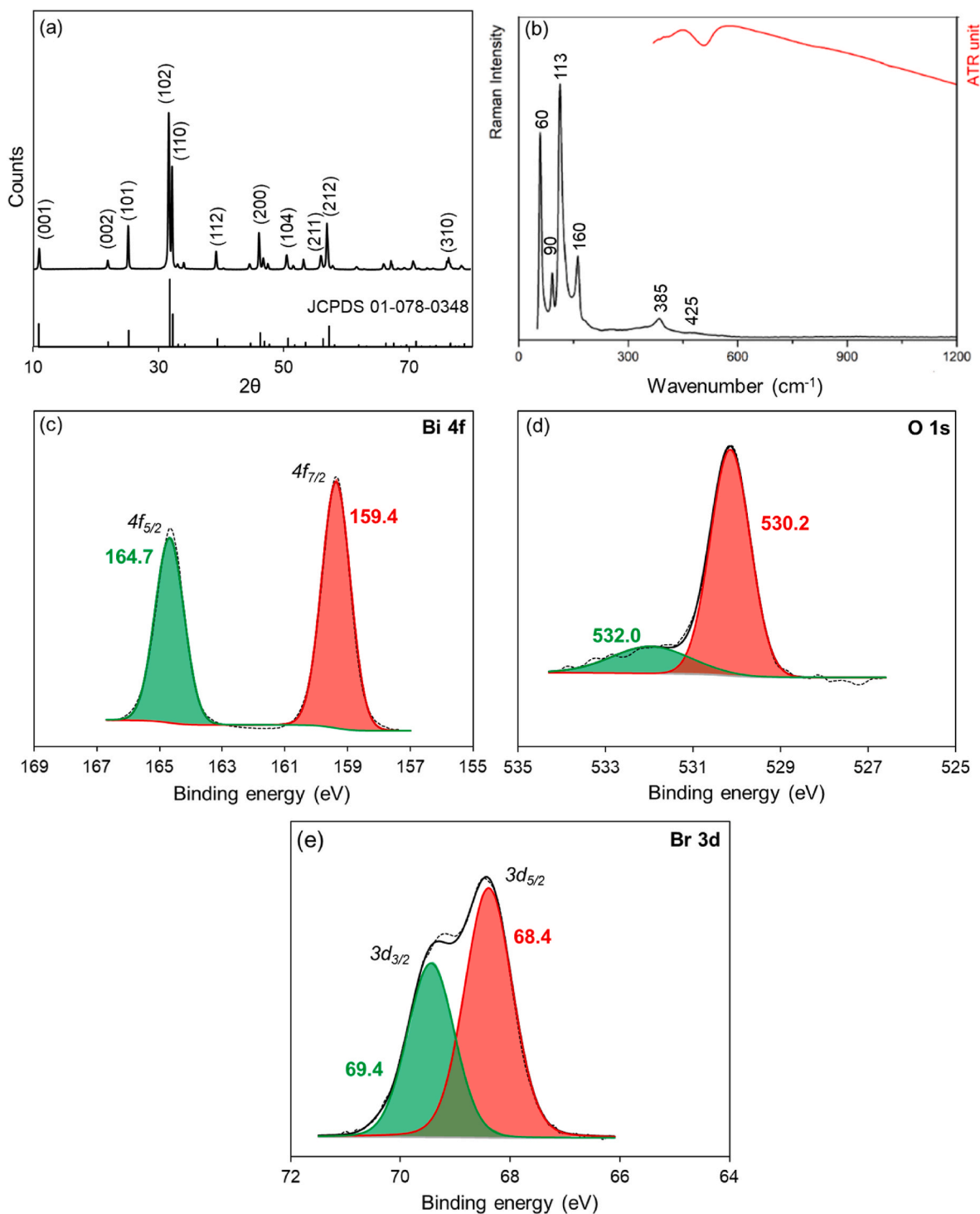

Fig. 1. (a) XRPD patterns of BiOBr powder compared to the reference (JCPDS 01-078-0348); (b) Raman and ATR spectra of BiOBr powder; (c) High Resolution (HR) XPS spectrum (dotted black lines) of Bi 4f; (d) HR XPS spectrum of O 1s; (e) HR XPS spectrum of Br 3d of BiOBr powder. Deconvolutions in sub-bands and the resulting fitted spectra (black lines) are also reported.

26.4, 26.4, 19.7, and 27.5 atom. %, respectively, after excluding the adventitious carbon peak (Figure S3b). HR spectrum of Bi 4f (Fig. 1c) presents two main peaks at 159.4 and 164.7 eV, ascribable to Bi 4f$_{7/2}$ and Bi 4f$_{5/2}$, respectively (Hu et al., 2022), confirming the presence of Bi^{3+} species at the BiOBr surface. The HR spectrum of O 1s (Fig. 1d) is composed of two contributions, centred at 530.2 and 532.0 eV, obtained by deconvolution in sub-bands. They can be associated to crystal lattice O atoms, *i.e.*, Bi-O, and surface hydroxyl groups. Eventually, the HR Br 3d spectrum (Fig. 1e) was deconvoluted in two main peaks at 68.4 and 69.4 eV, corresponding to Br 3d$_{5/2}$ and Br 3d$_{3/2}$ (Liu et al., 2014).

Unlike most of the literature on BiOBr, the N$_2$ adsorption/desorption isotherm of BiOBr at −196 °C (Figure S4) is II-Type, indicating non-porous or macroporous characteristics (Bi et al., 2023). SSA, computed by BET equation (2-parameters), is approximately 5 m^2 g^{-1}.

Point of zero charge (pH$_{pzc}$) is a key parameter to rationalize the photocatalyst behaviour, as it plays a key role in pollutants' adsorption capacity in aqueous medium. When the pH values are below the pH$_{pzc}$, the material surface becomes positively charged, thereby attracting anions. Conversely, when the pH values are higher than the pH$_{pzc}$, the surface becomes rich in negative charges, attracting cations (Falletta et al., 2023). The pKa values of the studied polyphenols are in 4.5–4.6 window, so at spontaneous pH (about 5 for GA, and 5.2 for 3,4,5-TMBA), the selected polyphenols are negatively charged, whereas the point of zero charge of BiOBr was found to be equal to *ca.* 5.5 (Figure S5a). According to these considerations, the adsorption of both studied polyphenols at the BiOBr surface should not be highly favoured, although the photodegradation results confirmed that the BiOBr surface was sufficiently positively charged to assure the polyphenols abatement, as demonstrated below.

BiOBr bandgap, computed by the Tauc plot (Figure S5b) of the UV-DR spectrum of BiOBr, corresponds to 2.55 eV, confirming the material capability to adsorb visible light.

Eventually, FESEM micrographs indicate that the BiOBr material exhibits an almost flower-like morphology, if inspected at low magnification (Fig. 2a). When the magnification is increased, even up to high resolution (Fig. 2b–d), it is evident that the ultimate morphology is more related to the presence of very thin *lamellae*, which in turn are composed by nanosheets, with a more or less irregular shape. Moreover, despite the shape, the mean thickness of the lamellae spans in the 25–50 nm range.

3.1.2. Alginate-based materials

To exploit alginate as environmentally friendly support, the pristine alginate spheres, magnetic particles, and the magnetic spheres were properly characterized.

As preliminary step, magnetic particles were studied through HR-TEM and XRPD. The morphology of the magnetic particles is depicted in the main section of Figure S6: the mean dimensions, roughly falling in the 20–60 nm size range, indicate that the Fe$_3$O$_4$ system is made up of nanoparticles (NPs) which are also *(i)* very thin and closed-packed each other and *(ii)* characterised by rough edges. If these NPs are inspected in deeper detail, it is evident that they are distinguished by high crystallinity (as also confirmed by the XRD analysis, *vide infra*), witnessed by the abundant crystalline fringes (see the main inset to Figure S6): the most frequent distance evidenced is ascribable to the (311) planes (JCPDS reference n. 19–0629) and confirmed by the "virtual" electron diffraction (reported in the inset to the inset to Figure S6 and obtained by calculating the FFT of the image portion highlighted by the arrow).

Figure S7 displays the obtained XRPD diffractogram. The detected 2θ peaks at *ca.* 30.2°, 35.6°, 43.5°, 54.2°, 56.8°, and 62.8° are indexed to
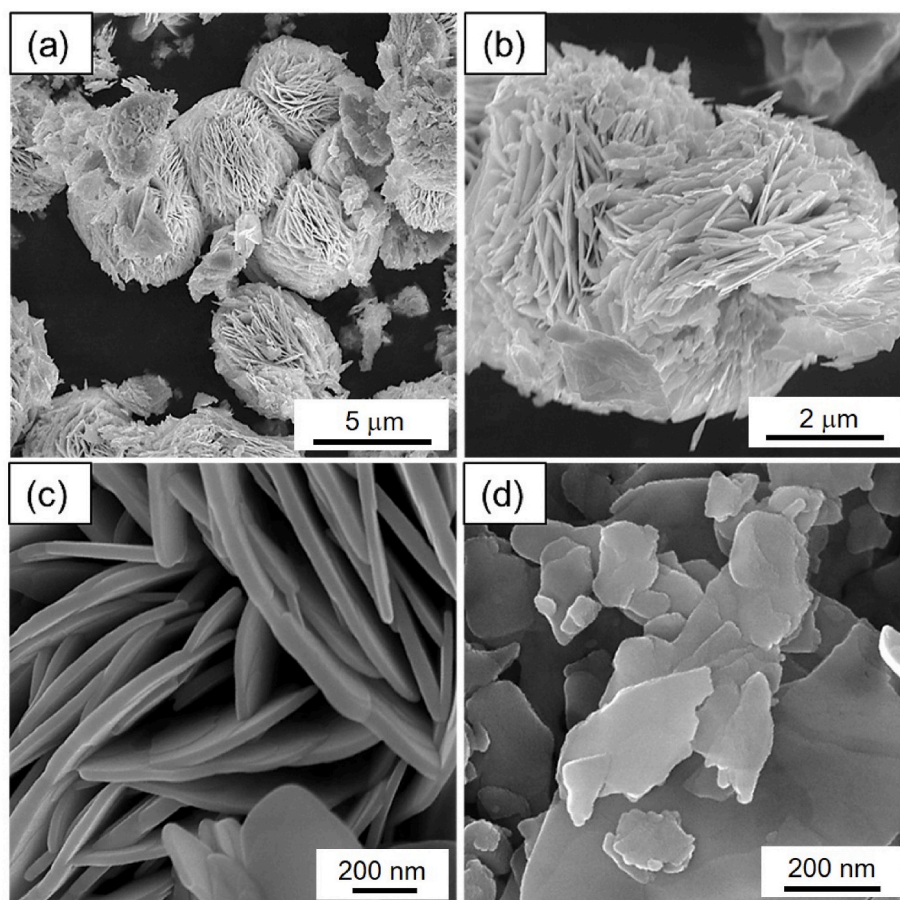

Fig. 2. BiOBr powder FESEM images.

the (220), (311), (400), (422), (511), and (440) planes of the magnetite, according to the JCPDS reference n. 19–0629 (Salem et al., 2013).

The main physico-chemical features of bare alginate spheres and alginate magnetic spheres were provided by targeted techniques. Images by optical microscope and FESEM are depicted in Figure S8. As for bare alginate, its optical microscope image reveals an homogeneous nature of the beads (Figure S8a), which appear opaque with the copresence of both smooth and rough external surfaces: these features are confirmed by the inspection by FESEM (Figure S8c), in which two morphologically different situations may be evidenced, roughly corresponding to regions in which the gelation process has proceeded to different extent (Ayarza et al., 2016). However, the most frequent situation corresponds to the highly gelled regions (*i.e.*, those in which the formation of a network has been brought about more effectively and we can observe interconnected "sheets" (inset to Figure S8c). When the magnetic components are added into the alginate spheres, their presence is massively evident even at
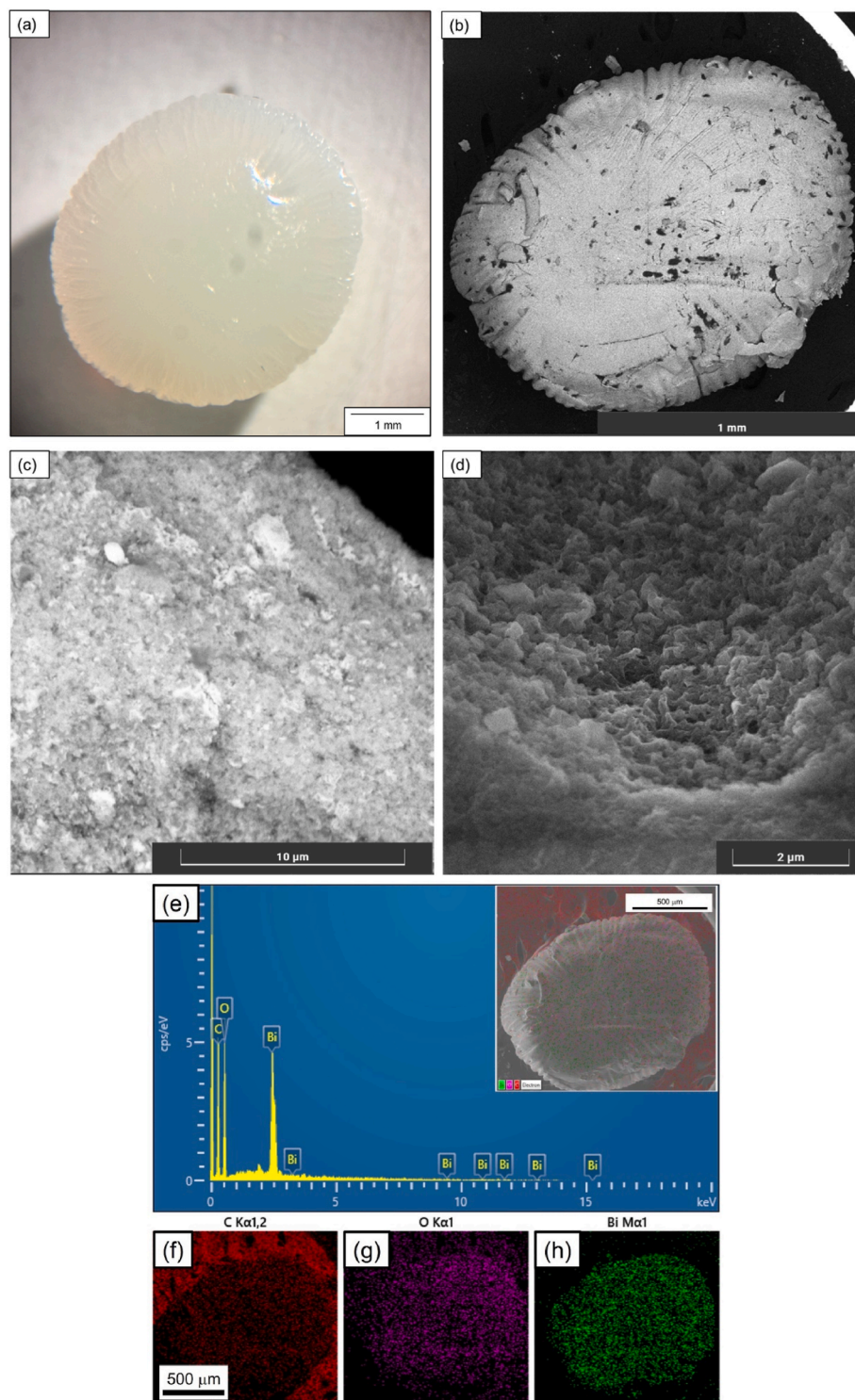

Fig. 3. Optical microscope (a), FESEM images (b–d) at different increasing magnifications, EDS spectrum with sum map as inset (e), elemental maps (f–h) referred, respectively, to C, O and Bi species (for all single element map, the same marker is represented only once) of the Bi^{3+}-modified alginate spheres.

macroscopic level: in the optical microscope image (Figure S8b) it is clearly observable the presence of frequent darker "islands", corresponding to magnetite. Moreover, the general morphology of this composite is quite different from that of bare alginate, as the interconnected sheets are now hardly evidenced (Figure S8d), leaving the floor to more compact and rough structure (even though here and there some sheets are still observable).

ATR FT-IR spectra of bare alginate spheres and the magnetic ones are displayed in Figure S9a. For both samples the most intense signal is a broad band attributable to the stretching modes of OH groups interacting by H bonding with water. Superimposed to this band are well recognizable the C-H stretching modes, at 2920 and 2850 cm^{-1}. Bare and magnetic alginate spheres present similar features also in the fingerprint region: as the bands attributable to the stretching modes of COO^- (symmetric at around 1595 cm^{-1} and asymmetric at around 1420 cm^{-1}) and a structured band in spectral range 1200-900 cm^{-1} due to $\nu(CO)$, $\nu(CC)$, $\delta(CCO)$ and $\delta(CC)$ modes (Fuks et al., 2006). The major difference between bare and magnetic alginate spheres are observed at low wavenumbers: for the second sample there is a broad band centred at 550 cm^{-1}, corresponding to the highest signal in magnetite spectrum.

TGA analyses (Figure S10) of the bare alginate spheres and the magnetic ones in the 30–800 °C window reveal four stages of mass loss without any evident difference between the two samples. The mass loss between 30 and *ca.* 150 °C corresponds to the desorption of water physisorbed onto the alginate surface. The main weight loss is detected in the 150–300 °C range and could be ascribed to the polymer degradation, in particular to the glycosidic bonds' destruction, according to Amirnejat et al., 2020. Finally, the third and fourth decomposition stages are detected in the 550–650 °C interval and identified as the $CaCO_3$ formation (Amirnejat et al., 2020).

In general, it was not possible to collect information on the point of zero charge of alginate-based spheres because of their high instability in alkaline conditions.

The Bi-modified alginate spheres were also characterized, and the results are described below.

The Bi^{3+}-modified alginate spheres were preliminary analysed by ICP to determine the Bi-loading corresponding to 8 wt%. Then, images by optical microscope and FESEM at different magnifications were collected (Fig. 3). The optical microscope investigation reveals similarities with those of bare alginate-based spheres (Fig. 3 and Figure S.8.a), in which the beads exhibit homogeneous macroscopic features. On the contrary, FESEM images put into evidence that at micro- and nanoscopic level the morphology becomes more and more heterogeneous (Fig. 3b), revealing rough surfaces rich in aggregated structures which, if inspected at high resolution (Fig. 3c and d), exhibit a nano-nature, made up of small particles quite stuck each other with a general possible presence of porosity. To assess the real presence of Bi species in this material, EDS analyses were run on the same particle, as reported in Fig. 3b: the relevant results, referred as the whole EDS spectrum, the general sum map (as inset) and those relative to the individual elements are reported in Fig. 3e–h. As it can be clearly observed, Bi species are present as expected, besides O and C. Bi and O species lie in the very same outer location on top of the inspected bead, indicating their strict bond, being C species located in an inner situation (the other high-density location of C species is due to the tape used to perform the FESEM measurement).

ATR-FTIR spectrum confirmed the modification induced by Bi incorporation into the alginate network (Figure S9). In fact, the stretching modes of COO^- groups show a shift of 20 cm^{-1} toward lower frequency with respect to that relative to the calcium alginate spheres, attributable to the high mass of Bi ions. In the spectrum of Bi^{3+}-modified alginate spheres there is a peak located at 1725 cm^{-1}, attributable to a partial protonation of carboxylate groups, (Papageorgiou et al., 2010) due to acidic behaviour of Bi^{3+} ions in water solution. TGA profile of Bi^{3+}-modified alginate spheres was similar to that of alginate spheres previously described (Figure S10a,c).

BiOBr/magnetic alginate spheres were studied as well. AAS was used

to determine the material composition. The results demonstrated that: *ca.* 38 wt% material is BiOBr, and 1 wt% is Fe_3O_4.

The bandgap, computed by the Tauc plot (Figure S11) of the UV-DR spectrum, corresponds to *ca.* 2.63 eV. This was in line with the presence of BiOBr on the composite, confirming its activity towards visible light.

Then, also in this case images by optical microscope and FESEM at different magnifications were collected (Fig. 4). It is worth noting that the co-presence of both magnetite and BiOBr besides alginate in the last examined beads leads to the following interesting morphological considerations: *(i)* the macroscopic features of the alginate are almost totally lost, as the sphere reported in Fig. 4a exhibits heterogenous outer features, being opaque, rich in "wrinkels" and appearing tougher than all the other investigated beads; *(ii)* as for the microscopic features, evidenced by means of FESEM and reported in Fig. 4b and c at increasing magnification, it might be put into evidence that there are almost no more "sheets", resembling the alginate features and, if any, they appear to be wrapped each other; *(iii)* the main morphological feature seems to be that of small aggregates (mean dimensions in the 3–6 μm, as evident in Fig. 4c). When we inspect the composite in the form of powder (obtained by a bead), the ultimate morphology resembles that of BiOBr, consisting of *lamellae* with a certain irregular shape, highly stacked together. (Figs. 4d and 2). As no specific indication about the presence of magnetite raised by the FESEM images, EDS analysis was resorted to confirm this feature: see Fig. 4e in which, besides Fe, all other elements have also been detected (with Cr species resulting from the sputtering procedure necessary to render the sample conductive for the FESEM investigation).

ATR-FTIR spectrum of BiOBr/magnetic alginate spheres (Figure S9) is very similar to that of the bare alginate sphere one. Also in this case, the acidic synthetic conditions during BiOBr formation cause a partial protonation of carboxylate groups and a signal at 1725 cm^{-1} is subsequently observed. At low wavenumbers, superimposed to the broad magnetite band, the band of BiOBr at 505 cm^{-1} is well recognizable. Eventually, the thermal study of these spheres was carried out through TGA analysis (Figure S10d), demonstrating a higher stability of these materials compared to the others due to the BiOBr-alginate interaction. For temperatures higher than 500 °C a gradual mass loss was additionally detected probably attributable to the material's active phase (BiOBr).

3.2. Polyphenols abatement

As previously reported, in this work, two model polyphenols (GA and 3,4,5-TMBA) were selected as target molecules due to their difficulty in being removed from the water matrix. The aim was to investigate the effect of the pollutants' structure on the materials' performance, so all abatement tests were conducted with each polyphenol individually in the ultrapure aqueous solutions to clearly identify the interactions between the studied polyphenol and adsorbent/photocatalyst.

At the beginning, the adsorption capacity of both bare alginate and magnetic alginate spheres was investigated towards GA.

Figure S12 reports the results obtained in terms of GA adsorption when 50 g L^{-1} bare alginate spheres are introduced into 100 mg L^{-1} GA solution in UW in the dark. After 3.5 h the maximum adsorption capacity is below 10% and a similar trend was also obtained when magnetic alginate spheres were employed in the same conditions (Figure S12). This behaviour underscores that the magnetite inclusion in the spheres does not affect the adsorption capacity of the easily recoverable support, but simply facilitates its recover after use (Video 1).

Based on these findings, with the aim to develop an easily recoverable material characterized by enhanced performances in polyphenols removal, two types of Bi-modified alginate spheres were explored: *i)* Bi^{3+}-modified alginate spheres, characterized by the exclusive presence of Bi^{3+} ions (instead of Ca^{2+}) at the surface and inside the alginate spheres, and *ii)* BiOBr/magnetic alginate spheres, whose preparation was optimized in this study for the first time. Unlike the traditional
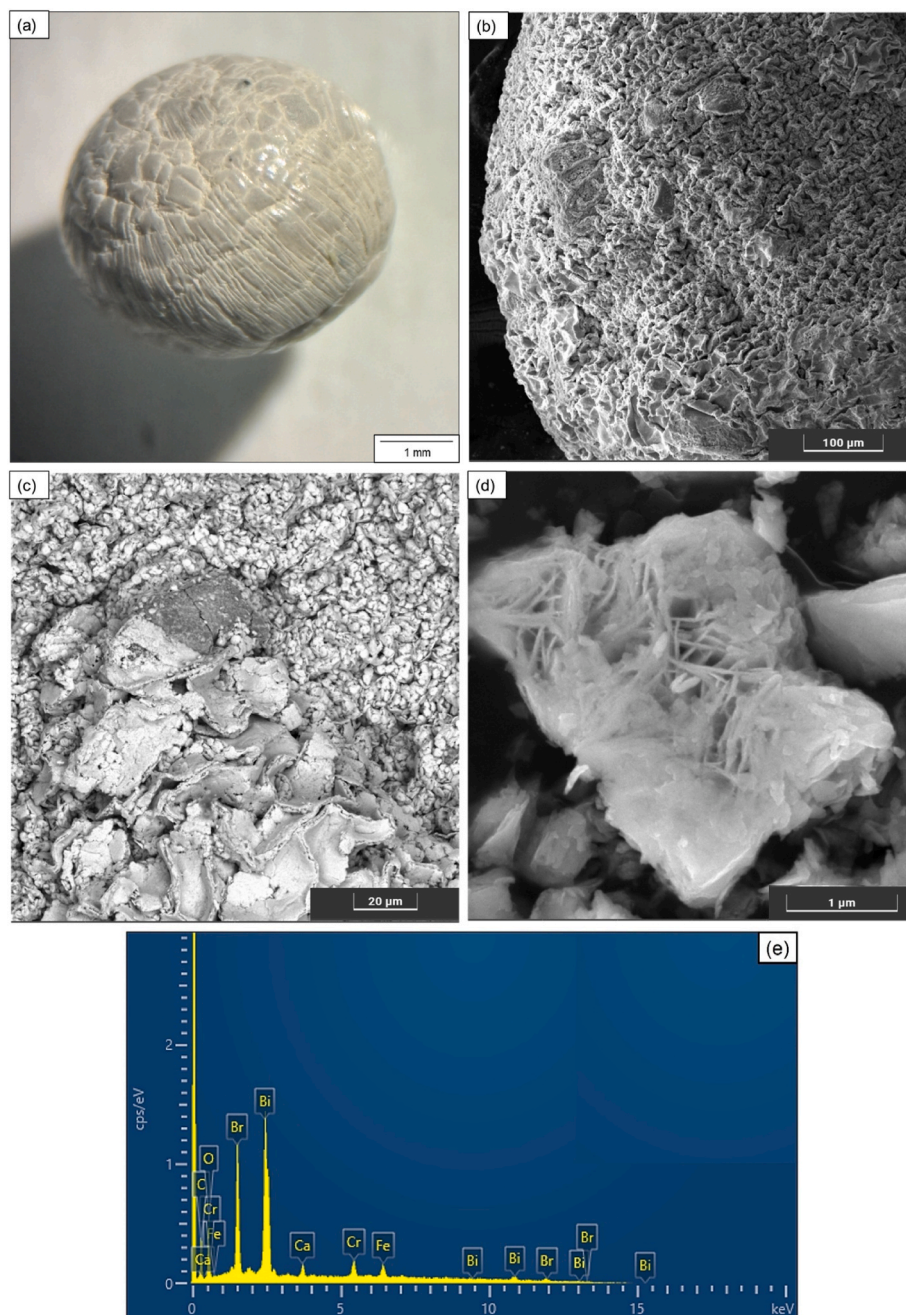
Fig. 4. Optical microscope (a), FESEM images at different magnifications (b, c: undamaged sphere; d: as a powder) and EDS spectrum (e) of BiOBr/magnetic alginate spheres.

procedures employing KBr as Br precursor for the semiconductor preparation, here CaBr$_2$ was selected necessarily, since it ensured the BiOBr layer growth onto the alginate spheres without any successive loss of BiOBr and without competitive BiOCl subproduct formation due to the presence of chlorine ions on the surface of alginate prepared by CaCl$_2$ (data not shown).

At first, both materials were tested in the adsorption of 100 mg L^{-1} GA or 3,4,5-TMBA at fixed spheres dosage (50 g L^{-1}). The Bi^{3+}-modified alginate spheres were more efficient than the BiOBr/magnetic ones in the selected polyphenols' adsorption (Fig. 5). More in detail, the former displayed *ca.* 80% and 20% adsorption capacity of GA and TMBA, respectively, within 180 min.

Differently, the BiOBr/magnetic alginate composite exhibited only a moderate ability to adsorb both polyphenols. This evidence could be

ascribed to the different exposition of the Bi^{3+} centres in the two materials, more available for Bi^{3+}-based spheres than for BiOBr-based ones, affecting their chelating capability towards the polyphenols' functional groups thanks to their well-exposed positive charges. More in detail, GA is more efficiently adsorbed than 3,4,5-TMBA under the same experimental conditions. Notably, 50% adsorption capacity for GA was reached within 180 min, whereas only a maximum of 20% adsorption was observed for 3,4,5-TMBA within the same timeframe. Based on these results, the different adsorption capacities of the composite spheres towards the two polyphenols were rationalized and schematized in Scheme 2. The different adsorption capability of the two Bi-modified materials can be reasonably attributed to two main factors: *i)* the different chelating ability of both Bi^{3+} centres and BiOBr species, *ii)* the different functional groups present in the aromatic ring of the two
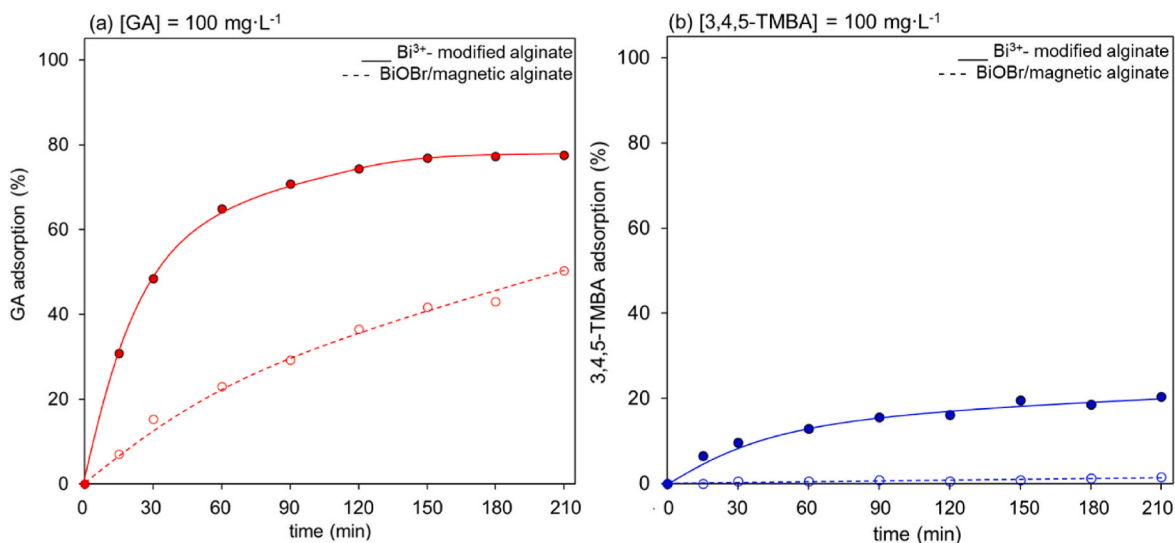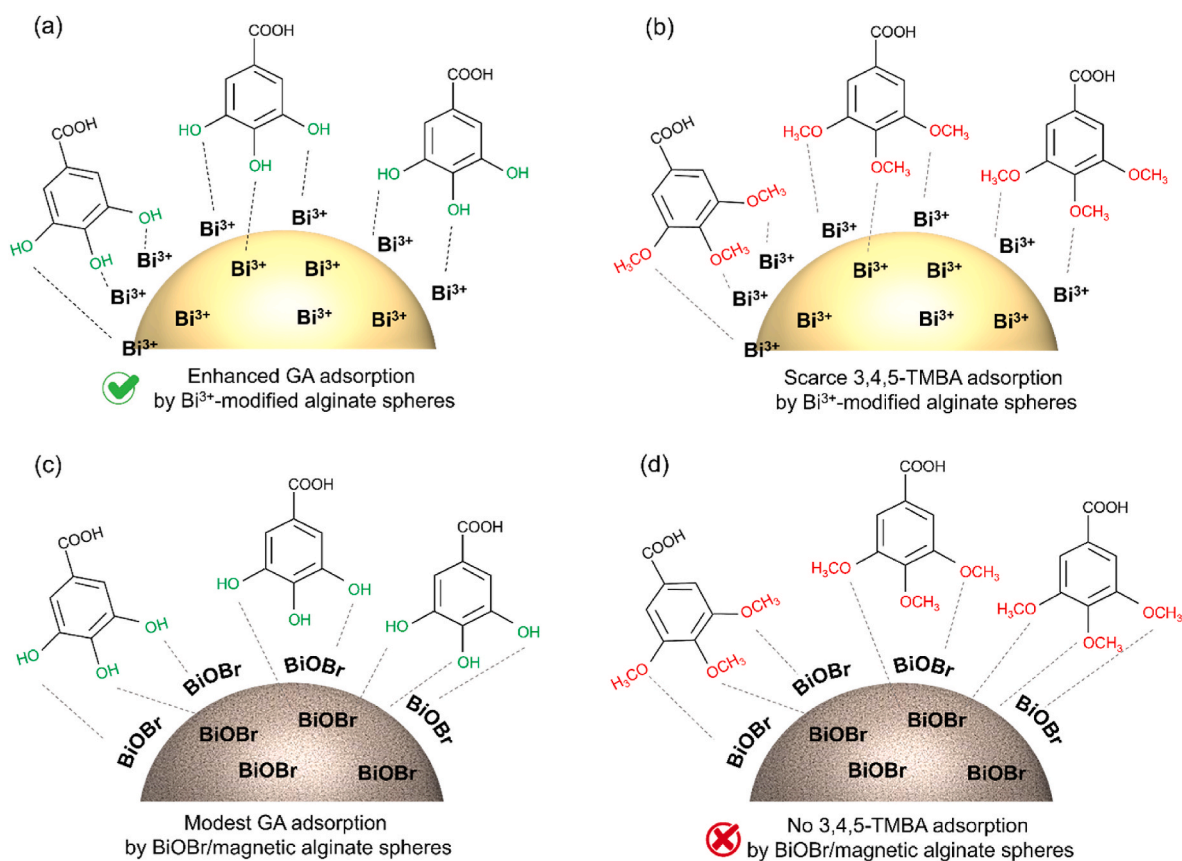
Fig. 5. Adsorption of GA and 3,4,5-TMBA (100 mg L^{-1}) under dark by 50 g L^{-1} Bi-based materials.

Scheme 2. Schematic representation of chelating centres of Bi-modified materials during the adsorption of GA and 3,4,5-TMBA.

molecules as. In fact, although in both molecular structures the aromatic rings are substituted with three organic groups in the same positions (3,4,5), in the case of GA, these groups are hydroxyl groups, whereas for 3,4,5-TMBA they are methoxy groups. Moreover, the Bi centres in BiOBr have a lower chelating capacity than Bi^{3+} ones, reducing the adsorption capability of the BiOBr-modified magnetic alginate materials. These preliminary findings revealed that the BiOBr/magnetic alginate spheres exhibit a certain polyphenol adsorption capacity, but it is not satisfactory for capturing large quantities of polyphenols. In contrast, Bi^{3+}-modified alginate spheres paved the way to a new category of polyphenols adsorbent materials. Unfortunately, so far, any attempt to desorb GA from the surface of the Bi^{3+}-modified beads has not led to significant results due to the poor stability of the alginate spheres under the conditions used.

However, the photocatalytic properties of BiOBr semiconductor (Luo et al., 2022; Wang et al., 2019a,b) can be exploited virtuously, employing BiOBr/magnetic alginate spheres for the polyphenols photodegradation under light irradiation.

As preliminary point, the photodegradation capacity of BiOBr powder towards the studied polyphenols was investigated. Figure S13 reports the results of GA and 3,4,5-TMBA photodegradation at different starting concentrations (10–100 mg L^{-1} interval) using variable BiOBr dosage (0.125 g L^{-1} - 0.500 g L^{-1} range).

Concerning GA, starting with a thorough examination of the semiconductor behaviour in the dark (adsorption), the adsorption percentage remains relatively low (*ca.* 10%), independently of the catalyst dosage and polyphenol concentration. Looking at the results of experiments carried out at the lowest pollutant concentration (10 mg L^{-1}), full GA abatement rate was achieved after 60 min. However, as the pollutant concentration increases, the reaction rate decelerated, and 100% abatement was not achieved after 180 min, indicating that a longer reaction time may be required. Specifically, at 50 mg L^{-1} GA concentration 90% maximum abatement was achieved, highlighting the influence of pollutant concentration on the reaction kinetics. It is possible to assume that in these conditions large amounts of byproducts produced during the reaction act, partially blocking the active sites. This is corroborated by the mineralization results: in fact, under solar light the mineralization percentages for a solution with an initial concentration of 50 mg L^{-1} in the presence of 0.500, 0.250, and 0.125 g L^{-1} BiOBr were 29, 15, and 12 %, respectively (Figure S14a). However, for a higher initial concentration of GA (100 mg L^{-1}) the percentages of mineralization decreased to 11% for 0.500 g L^{-1}, 7% for 0.250 g L^{-1}, and 2% for 0.125 g L^{-1} BiOBr (Figure S14b).

Concerning 3,4,5-TMBA, the adsorption was very minimal, never exceeding 5%, irrespectively to the pollutant concentration and catalyst dosage (Figure S13). In addition, in the experiments performed under solar light, BiOBr was found to be able to almost abate the studied pollutant fully across all experimental conditions. For low initial pollutant concentration (10 mg L^{-1}) 100% pollutant abatement was achieved within 60 min for the catalyst dosages of 0.50 and 0.25 g L^{-1}. Reducing the catalyst concentration at 0.125 g L^{-1}, a complete abatement was attained after 90 min. As the initial pollutant concentration increases, the reaction rate gradually decreased. At a pollutant concentration of 50 and 100 mg L^{-1}, a complete abatement was reached only after 150 min with a catalyst powder concentration of 0.50 g L^{-1}, whereas using 0.125 g L^{-1} BiOBr, no full abatement of the polyphenol was achieved. HPLC chromatograms revealed the presence of the peak related to the target pollutant, as well as additional peaks associated to transformation products, which gradually decreased over time, confirming the photodegradation process occurrence. These findings confirmed the solar driven photocatalytic capabilities of the BiOBr powder for 3,4,5-TMBA degradation. In this case, evaluations of BiOBr mineralization capacity were also conducted. Under solar light conditions, for the tests carried out by an initial polyphenol concentration of 50 mg L^{-1}, the percentages of mineralization corresponded to 45, 32 and 29% for 0.500, 0.250, and 0.125 g L^{-1} BiOBr, respectively (Figure S14a). For a higher initial concentration of pollutant (100 mg L^{-1}), the percentages of mineralization under solar light slightly decreased compared to the previous ones, as expected: they corresponded to 42% for 0.500 g L^{-1}, 29% for 0.250 g L^{-1}, and 27% for 0.125 g L^{-1} BiOBr catalyst (Figure S14b).

Then, supported by these encouraging results, the performances of BiOBr/magnetic alginate spheres were largely explored.

Preliminarily, the adsorption and photodegradation capacity of the bare magnetic alginate spheres were checked in the presence of the lowest and highest concentrations of each single polyphenols investigated (10 and 100 mg L^{-1}, respectively). As illustrated in Figure S15, both adsorption and photodegradation activity of bare magnetic spheres was minimal. Only approximately 10% polyphenol abatement was achieved after 180 min light exposure, regardless of the starting polyphenol concentration.

Subsequently, the BiOBr/magnetic alginate composites' photodegradation activity was explored under solar light. Various dosages of the composite spheres (ranging from 10 to 50 g L^{-1}) and pollutant concentrations (from 10 to 100 mg L^{-1}) were investigated: the obtained results are summarized in Fig. 6.

To compare the performance of the BiOBr powder with that supported onto magnetic alginate spheres at the same dosage, a preliminary test involving dark adsorption followed by photodegradation of 10 mg L^{-1} GA in the presence of the appropriate amount of BiOBr/magnetic alginate spheres (resulting in the final BiOBr active phase dosage of 0.5 g L^{-1}) was conducted. The obtained results (Figure S16) indicate that, in contrast to the results obtained when BiOBr is used in powder form (Figure S13), when BiOBr was immobilized onto the magnetic alginate spheres under these conditions, the composite spheres exhibited low adsorption capacity during the initial 30 min in the dark and negligible photocatalytic activity (only 18% degradation after 180 min solar irradiation). This outcome suggests that in the composite material BiOBr is not only present on the magnetic alginate spheres' surface, but also within the internal part of the spheres, according to FESEM results (Fig. 4). Moreover, the BiOBr-alginate interaction negatively affect the photocatalytic properties of the semiconductor limiting at the time the exposition of the photocatalyst surface area towards light and pollutants.

Taking in mind these findings, a series of experiments were conducted at various pollutants initial concentrations (ranging from 10 to 100 mg L^{-1}) in the presence of different dosages of BiOBr/magnetic alginate spheres (5–10 g L^{-1} window, *i.e.* 1.9–3.8 g L^{-1} BiOBr, Fig. 6).

In general, as expected, the polyphenols abatement capacity of the BiOBr-modified spheres decreased as the pollutant concentration increased and enhanced with the spheres' dosage. Moreover, the use of large amounts of BiOBr-modified spheres led to a certain percentage of polyphenols adsorption higher for GA than for 3,4,5-TMBA for the same reasons discussed above.

Concerning GA abatement, the best results were obtained for large spheres dosage (50 or 100 g L^{-1}), achieving 100%, 92%, 70% GA removal for polyphenol concentrations of 10, 50 and 100 mg L^{-1}, respectively.

As previously described, the BiOBr-alginate interaction and the lower exposed surface of the semiconductor to the environment reduce the 3,4,5-TMBA abatement.

However, the findings permit to conclude that the polyphenols abatement by the BiOBr magnetic spheres is due to a combination of phenomena, occurring on the composites' surface thanks to the double role of the semiconductor: *i)* chelation by the Bi-centres of the semiconductor, and *ii)* photodegradation by BiOBr activity. More in detail, it is possible to hypothesize that the BiOBr magnetic spheres act as a "*concentrate and destroy*" device capable to degrade gradually also the pollutant adsorbed on its surface.

As carried out for BiOBr powders, it is crucial to address the evaluation of the mineralization capacity of the composite material. This aspect delves deeper into the extent to which the polyphenols are broken down into simpler molecules, providing insights into the long-term consequences of the degradation process, *i.e.*, the overall environmental impact. Unfortunately, the slight degradation of the alginate shell of the spheres, compromised the evaluation of their mineralization capacity by TOC analyses.

According to this evidence, although the great advantages of the magnetic recovery and the promising capacity in abating polyphenols of the BiOBr/magnetic alginate spheres, some major drawbacks still need to be overcome. On one hand, the time-dependent biodegradability of alginate polymer must be considered when the material has to be used multiple times. This leads to the loss of the supported catalyst in solution that is not toxic, but could be an unwanted feature. This point is fundamental to be considered to furtherly optimize the composite for the real application. On the other hand, the activity of the composite strongly depends on the nature of the treated polyphenol. Regarding this latter point, it is fundamental to underline that an additional scenario deserving to be investigated is the copresence of polyphenols in the aqueous solution, approaching the composition of a real OMWW.
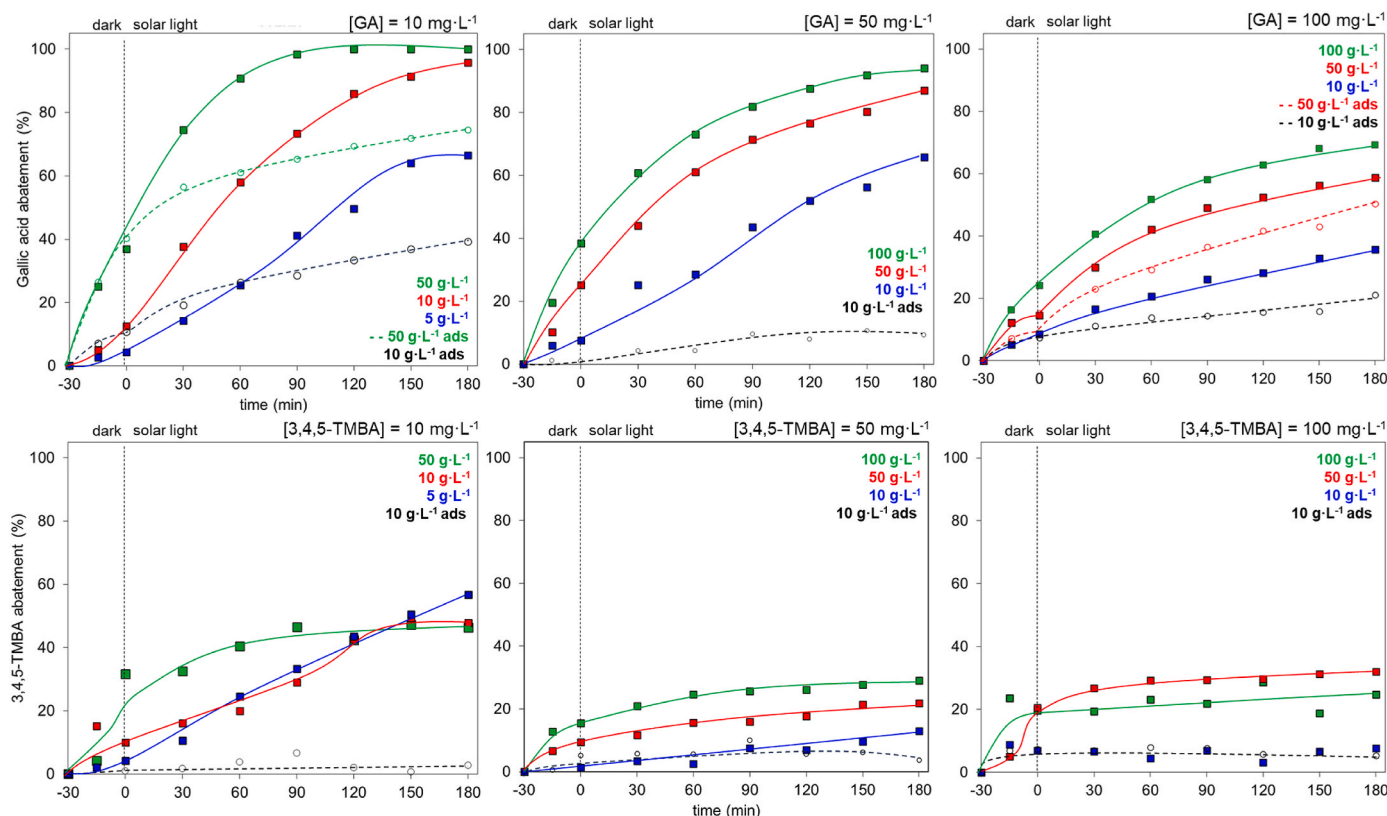
Fig. 6. Photodegradation tests of gallic acid and 3,4,5-TMBA with different dosages of BiOBr/magnetic alginate spheres under dark and solar irradiation (35 W m^{-2}).

Preliminary experiments are revealing that an interesting framework to be explored occurs depending on solution pH, polyphenol stability, *etc.*

3.3. Coupled experiments of polyphenols' adsorption/photodegradation

Based on the previously discussed results, the focus was on maximizing the capture of polyphenols and subsequently degrading any remaining traces in the solution. These tests were performed using GA solutions, as its structure is more suitable for this type of treatment.

In this context, at first 500 and 1000 mg L^{-1} GA were treated using Bi^{3+}-modified spheres (100 g L^{-1}) in dark (with the final purpose of recovering/adsorbing the most part of GA present in solution) and then with BiOBr/magnetic alginate spheres (100 g L^{-1}) under solar light
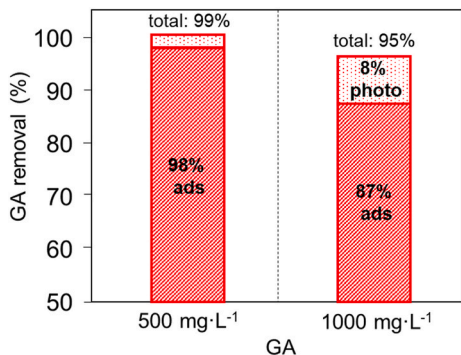

Fig. 7. Results of the coupled experiments of adsorption/photodegradation of gallic acid.
Step 1 (ads): Adsorption of gallic acid (GA) in the presence of 100 g L^{-1} Bi^{3+}-modified alginate spheres for 210 min under dark. Step 2 (photo): Photodegradation of the resulting GA solution in the presence of 100 g L^{-1} BiOBr/magnetic alginate spheres for 210 min under solar light irradiation (35 W m^{-2}).

irradiation (for photodegrading the traces of GA remained in solution) in sequence. Fig. 7 summarizes the obtained results. After 210 min in the dark, Bi^{3+}-modified spheres were able to adsorb 98% and 87% initial polyphenol, respectively. After this adsorption phase, replacing Bi^{3+}-modified spheres with BiOBr/magnetic alginate composites, after 210 min under solar light the remaining GA traces in solution were degraded. Finally, in total the coupled approach leads to the abatement of 100% and 95% polyphenol in solution.

These findings demonstrate the effectiveness of the combined adsorption and photocatalysis approach for capturing large amount of GA and degrading the remaining traces in solution. It is important to underline that the large amount of GA adsorbed on Bi^{3+}-modified spheres could be properly treated to desorb the polyphenol, and recover it in a circular economy perspective.

3.4. Antibacterial activity

The antibacterial activity of the prepared samples was gained by disk diffusion method against the microorganisms *Escherichia coli*, *Staphylococcus aureus*, *Listeria ivanovii*, *Candida alibicans* and *Aspergillus niger* (Table 1).

In general, no inhibition zones were shown on the BiOBr powder, regardless the microbial strain tested. In case of alginate and magnetite alginate spheres, a slight antibacterial activity was proved only against *E. coli* and *L. ivanovii*, respectively. The most significant antibacterial effect was revealed in the case of Bi^{3+}- modified alginate spheres against *E. coli*, *L. ivanovii* and *S. aureus*, whereas no antifungal inhibition was observed.

Concerning antibacterial activity of Bi-based materials investigated so far, Das et al., (2020) confirmed the antibacterial properties of Bi-NPs MIC against *E. coli* and *S. aureus*. In the study of Alli et al., (2022) MBC values for the quaternary trimethyl chitosan-stabilized by bismuth nanoparticles (QTMC-BiNPs) of *E. coli* 31.25 μg mL^{-1} and S. aureus

Table 1
Summary of the values of inhibition zones obtained on the BiOBr powder and the alginate-based materials for the tested bacteria.

Code[a]	Escherichia coli (mm)	Staphylococcus aureus (mm)	Listeria ivanovii (mm)	Aspergillus niger (mm)	Candida albicans (mm)
BiOBr powder	N[a]	N	N	N	N
bare alginate spheres	7 ± 1	N	N	N	N
magnetite alginate spheres	N	N	8 ± 1	N	N
Bi^{3+} modified alginate spheres	13 ± 1	14 ± 1	17 ± 1	N	N
BiOBr/magnetic alginate spheres	10 ± 1	12 ± 1	11 ± 1	N	N

[a] disk diameter is of about 6 mm; N = no inhibition zone.

500.00 μg mL^{-1} were estimated against, respectively. Bari et al., (2022) revealed that doped Bi_2O_3 has an improved bactericidal synergism and activity against *S. aureus*. Apart from this, doped Bi_2O_3 showed substantial antibacterial efficacy against *S. aureus* as compared with *E. coli*, according to our study. It is generally known that cell walls of Gram-negative bacteria have a more complicated structure than the Gram-positive ones, which can lead to different sensitivity to Bi.

The cell surface layer of each bacterial strain is distinctive, and the composition of bacterial membranes varies considerably, affecting their relative permeability. Inorganic nanoparticles have been demonstrated to induce bacterial toxicity through a number of mechanisms, including the induction of reactive oxygen species (such as hydroxyl radicals), lipid peroxidation, enzyme inhibition, oxidative stress, proteolysis, and lysis of the cell membrane. Additionally, they have been shown to affect bacterial genetics at the expression level (Li et al., 2022; Bari et al., 2022; Bakeke and Oladipo, 2024). It seems reasonable to suggest that there are two possible mechanisms of the antibacterial activity for the studied sample may entail the generation of free radicals, which can induce oxidative stress and consequently damage essential cellular organelles, proteins, and membrane permeability, thereby disrupting the osmotic potential. Furthermore, direct contact between Bi^{3+} and the microbial cell wall, as well as interaction with cellular phospholipids and glycolipids, can disrupt lipid and protein metabolism, ultimately leading to the breakdown of cell membranes (Bisht et al., 2022; Bari et al., 2022; Mustafa et al., 2022).

An additional viewpoint worth discussing is the toxicity, even though it is controversial because only a few studies have been dedicated to this issue.

If, on one hand, many papers have been dedicated to the investigation of bismuth nanoparticles toxicity, the literature lacks studies on that of Bi^{3+} ions and BiOBr. In general, bismuth is a metal well known for its low toxicity.

Although 15 g can be tolerated by an adult, the exposition to bismuth for long time may cause side effects and even toxicity to human subjects. The extent of bismuth toxicity depends on individual cases: type of bismuth compounds and the dose. However, it is still not clear why only some individuals develop toxicity to bismuth.

Thanks to their low toxicity, bismuth and its derivatives are widely employed in the medical and biomedical sectors. Additionally, bismuth has been used in the production of pharmaceutical products for the treatment of gastrointestinal disorders, hypertension, and syphilis. In addition, one of the main research areas of Bi NPs is cancer therapy (Stewart et al., 2016; Zhou et al., 2019; Hernandez-Delgadillo et al., 2018; Fan et al., 2012). Recently, the use of bismuth in nanosized form has been widely expanded in recent years in various domains, such as X-ray radiotherapy, biosensors, heavy-metal ion detectors, antimicrobial formulations, combined cancer therapy, bioimaging, and tissue engineering (Shahbazi et al., 2020). However, as with other metal nanoparticles, when bismuth is used in nanosized dimensions, it raises serious concerns about *in vivo* toxicity (Mishra et al., 2017). It is speculated that, like many other types of nanomaterials, Bi NPs usually possess dose-dependent adverse biological effects, and their cytotoxicity is largely dependent on particle diameter, charge, and surface modifications (Ai et al., 2011). Concerning BiOBr, only a few toxicity studies are reported. By way of example, Zhao et al. tested the BiOBr toxicity on

rye seeds (Zhao et al., 2022). After 7 days of cultivation at 25 °C the stalks grew quite regularly, demonstrating the low toxicity of the material. Gao and coworkers compared the BiOBr and TiO_2 NPs toxicological effects on human HaCaT cells, demonstrating that both NPs provoke concentration-dependent cytotoxicity by disturbing cell cycle and inducing cell apoptosis (Gao et al., 2015). However, BiOBr exhibited lower toxicity than TiO_2, confirming the extraordinary properties of this material.

4. Conclusions

In summary, this study proposes a novel approach for polyphenols abatement from water matrices using advanced easily recoverable bio-based materials made of magnetic alginate beads properly modified with Bi^{3+} centres or BiOBr.

These materials are designed to be cost-effective and environmentally efficient, providing an alternative to traditional solutions. Bi^{3+}-modified alginate spheres exhibited high adsorption features towards the investigated target molecules (gallic acid and 3,4,5-trimethoxybenzoic acid) thanks to higher chelating capability of Bi^{3+} compared to BiOBr. Moreover, the hydroxyl groups of gallic acid are responsible for a greater interaction with the metal centres than the methoxy groups of 3,4,5-trimethoxybenzoic acid. In contrast, the photocatalytic properties of BiOBr-modified magnetic beads permitted to achieve promising results in the polyphenols photodegradation under solar light. Focusing the attention on gallic acid abatement, the features of both Bi-based materials were exploited into a two-step process: *i)* adsorption of gallic acid present in large amount on solution (500 or 1000 g L^{-1}) by Bi^{3+}-modified alginate spheres, and *ii)* photodegradation of the remaining traces by solar light in the presence of BiOBr-modified alginate composites. Both materials were easily removed from the solution by the use of a magnet.

In line with the circular economy goal, this work *i)* paves the way for an innovative approach to the easy adsorption of polyphenols to water to reuse and the subsequent degradation of these molecules as traces in solution, and *ii)* meets some of the 169 Sustainable Development Goal (SDG) targets of the United Nations, in particular those related to "Clean Water and Sanitation" (SDG 6), "Responsible Consumption and Production" (SDG 12) and "Life on Land" (SDG 15).

Further investigations are ongoing to evaluate the performance of these promising materials in the presence of real OMWW to propose this new generation of eco-friendly bismuth-modified alginate spheres in real scenarios.

CRediT authorship contribution statement

Melissa G. Galloni: Writing – original draft, Methodology, Formal analysis, Data curation. **Vasilissa Nikonova:** Investigation, Formal analysis, Data curation. **Giuseppina Cerrato:** Validation, Software, Investigation, Data curation. **Alessia Giordana:** Investigation, Formal analysis, Data curation. **Pavel Pleva:** Investigation, Formal analysis, Data curation. **Petr Humpolicek:** Methodology, Investigation, Data curation. **Ermelinda Falletta:** Writing – review & editing, Writing – original draft, Supervision, Project administration, Funding acquisition, Data curation, Conceptualization. **Claudia L. Bianchi:** Writing – review & editing, Validation, Supervision, Resources, Funding acquisition.

Declaration of competing interest

The authors declare that they have no known competing financial interests or personal relationships that could have appeared to influence the work reported in this paper.

Data availability

Data will be made available on request.

Appendix A. Supplementary data

Supplementary data related to this article can be found at https://doi.org/10.1016/j.jenvman.2024.122365.

References

Abid, N., Ali Masmooudi, M., Megdiche, M., Barakat, A., Ellouze, M., Chamkha, M., Ksibi, M., Sayadi, S., 2022. Biochar from olive mill solid waste as an eco-friendly adsorbent for the removal of polyphenols from olive mill wastewater. Chem. Eng. Res. Des. 181, 384–398. https://doi.org/10.1016/j.cherd.2022.02.029.

Abakar, M.A.A., Khan, S.B., 2024. Alginate-wrapped NiO-ZnO nanocomposites-based catalysts for water treatment. J. Exp. Nanosci. 19 (1) https://doi.org/10.1080/17458080.2024.2375787.

Ai, K., Liu, Y., Yuan, Q., He, Y., Lu, L., 2011. Large-Scale synthesis of Bi$_2$S$_3$ nanodots as a contrast agent for in vivo X-ray computed tomography imaging. Adv. Mater. 23, 4886–4891. https://doi.org/10.1002/adma.201103289.

Alli, Y.A., Adewuyi, S., Bada, B.S., 2022. Quaternary trimethyl chitosan chloride capped bismuth nanoparticles with positive surface charges: catalytic and antibacterial activities. J Clust Sci 33, 2311–2324. https://doi.org/10.1007/s10876-021-02156-8.

Al-Qodah, Z., Al-Zoubi, H., Hudaib, B., Omar, W., Soleimani, M., Abu-Romman, S., Frontistis, Z., 2022. Sustainable vs. conventional approach for olive oil wastewater management: a review of the state of the art. Water 14, 1695. https://doi.org/10.3390/w14111695.

Alver, E., Metin, A.U., Brouers, F., 2020. Methylene blue adsorption on magnetic alginate/rice husk bio-composite. Int. J. Biol. Macromol. 154, 104–113. https://doi.org/10.1016/j.ijbiomac.2020.02.330.

Amirnejat, S., Nosrati, A., Javanshir, S., 2020. Superparamagnetic Fe$_3$O$_4$@Alginate supported L-arginine as a powerful hybrid inorganic–organic nanocatalyst for the one-pot synthesis of pyrazole derivatives. Appl. Organomet. Chem. 34 (10), e5888 https://doi.org/10.1002/aoc.5888.

Askarieh, M., Farshidi, H., Rashidi, A., Pourreza, A., Alivand, M.S., 2022. Comparative evaluation of MIL-101(Cr)/calcium alginate composite beads as potential adsorbents for removing water vapor from air. Sep. Purif. Technol. 291, 120830 https://doi.org/10.1016/j.seppur.2022.120830.

Atthanaphanit, A., Supaphol, P., Tamura, H., Tokura, S., Rujiravanit, R., 2010. Wet-spun alginate/chitosan whiskers nanocomposite fibers: preparation, characterization and release characteristic of the whiskers. Carbohydr. Polym. 79, 738–746. https://doi.org/10.1016/j.carbpol.2009.09.031.

Ayarza, J., Coello, Y., Nakamatsu, J., 2016. SEM–EDS study of ionically cross-linked alginate and alginic acid bead formation. Int. J. Polym. Anal. Char. 22 (1), 1–10. https://doi.org/10.1080/1023666X.2016.1219834.

Ayed, S.B., Mansour, L., Vaiano, V., Harrath, A.H., Ayari, F., Rizzo, L., 2023. Magnetic Fe$_3$O$_4$-natural iron ore/calcium alginate beads as heterogeneous catalyst for Novacron blue dye degradation in water by (photo)Fenton process. J. Photochem. Photobiol. Chem. 438, 114566 https://doi.org/10.1016/j.jphotochem.2023.114566.

Bari, A., Ikram, M., Haider, A., Ul-Hamid, A., Haider, J., Shahzadi, I., Nazir, G., Shahzadi, A., Imran, M., Ghaffar, A., 2022. Evaluation of bactericidal potential and catalytic dye degradation of multiple morphology based chitosan/polyvinylpyrrolidone-doped bismuth oxide nanostructures. Nanoscale Adv. 4, 2713–2728. https://doi.org/10.1039/D2NA00105E.

Bakeke, H., Oladipo, A.A., 2024. Antimicrobial activity of biogenic-synthesized novel bimetallic nanospinel LiCu-ferrite particles: experimental and computational studies. J. Mol. Struct. 1296 (1), 136823 https://doi.org/10.1016/j.molstruc.2023.136823.

Benettayeb, A., Ghosh, S., Usman, M., Seihoub, F.Z., Sohoo, I., Chia, C.H., Sillanpaa, M., 2022. Some well-known alginate and chitosan modifications used in adsorption: a review. Water 14 (9), 1353. https://doi.org/10.3390/w14091353.

Bhachu, D.S., Moniz, S.J.A., Sathasivam, S., Scanlon, D.O., Walsh, A., Bawaked, S.M., Mokhtar, M., Obaid, A.Y., Parkin, I.P., Tang, J., Carmalt, C.J., 2016. Bismuth oxyhalides: synthesis, structure and photoelectrochemical activity. Chem. Sci. 7, 4832–4841. https://doi.org/10.1039/C6SC00389C.

Bi, F., Li, Z., Fu, X., Zhou, B., Li, H., Zhao, L., Xiao, S., Wang, L., Gai, G., Dong, X., 2023. One-Pot synthesis of BiOBr microspheres with effective visible-light photocatalytic performance for wastewater treatment. J. Mater. Sci. Mater. Electron. 34, 1694. https://doi.org/10.1007/s10854-023-11129-8.

Bisht, N.S., Tripathi, A.H., Upadhyay, S.K., Sahoo, H.G., Mehta, S.P.S., Dandapat, A., 2022. A facile synthesis of palladium nanoparticles decorated bismuth oxybromide nanostructures with exceptional photo-antimicrobial activities. Colloids Surf. B Biointerfaces 217, 112640. https://doi.org/10.1016/j.colsurfb.2022.112640.

Buran, T.J., Sandhu, A.K., Li, Z., Rock, C.R., Yang, W.W., Gu, L., 2014. Adsorption/desorption characteristics and separation of anthocyanins and polyphenols from blueberries using macroporous adsorbent resins. J. Food Eng. 128, 167–173. https://doi.org/10.1016/j.jfoodeng.2013.12.029.

Cao, L., Ma, D., Zhou, Z., Xu, C., Cao, C., Zhao, P., Huang, Q., 2019. Efficient photocatalytic degradation of herbicide glyphosate in water by magnetically separable and recyclable BiOBr/Fe$_3$O$_4$ nanocomposites under visible light irradiation. Chem. Eng. J. 368, 212–222. https://doi.org/10.1016/j.cej.2019.02.100.

Chang, C.-F., Tseng, I.-P., 2013. Degradation of phenol by using magnetic photocatalysts of titania. Water Sci. Technol. 67 (7), 1434–1441. https://doi.org/10.2166/wst.2013.669.

Chen, X., Qiao, L., Zhao, R., Wu, J., Gao, J., Li, L., Chen, J., Wang, W., Galloni, M.G., Scesa, F.M., Chen, Z., Falletta, E., 2023. Recent advances in photocatalysis on cement-based materials. J. Environ. Chem. Eng. 11 (2), 109416 https://doi.org/10.1016/j.jece.2023.109416.

Cordeiro, E.de S., Scaratti, G., de Souza, D.C.S., Nickel, C.D.M., Josè, H.J., Moreira, R. de F.P. M., De Noni Junior, A., 2024. Red mud as catalyst for the treatment of pharmaceuticals compounds by advanced oxidation processes – a review. Environ. Nanotechnol. Monit. Manag. 21, 100938 https://doi.org/10.1016/j.enmm.2024.100938.

Das, P.E., Majdalawieh, A.F., Abu-Yousef, I., Narasimhan, S., Poltronieri, P., 2020. Use of A Hydroalcoholic extract of moringa oleifera leaves for the green synthesis of bismuth nanoparticles and evaluation of their anti-microbial and antioxidant activities. Materials 13 (4), 876. https://doi.org/10.3390/ma13040876.

Davies, J.E.D., 1973. Solid state vibrational spectroscopy—III[1] the infrared and Raman spectra of the bismuth(III) oxide halides. J. Inorg. Nucl. Chem. 35 (5), 1531–1534. https://doi.org/10.1016/0022-1902(73)80242-8.

Della Pina, C., Rossi, M., Ferretti, A.M., Ponti, A., Lo Faro, M., Falletta, E., 2012. One-pot synthesis of polyaniline/Fe$_3$O$_4$ nanocomposites with magnetic and conductive behaviour. Catalytic effect of Fe$_3$O$_4$ nanoparticles. Synth. Met. 162 (24), 2250–2258. https://doi.org/10.1016/j.synthmet.2012.10.023.

Djellabi, R., Giannantonio, R., Falletta, E., Bianchi, C.L., 2021. SWOT analysis of photocatalytic materials towards large scale environmental remediation. Current Opinion in Chemical Engineering 33, 100696. https://doi.org/10.1016/j.coche.2021.100696.

Ena, A., Pintucci, C., Carlozzi, P., 2012. The recovery of polyphenols from olive mill waste using two adsorbing vegetable matrices. J. Biotechnol. 157 (4), 573–577. https://doi.org/10.1016/j.jbiotec.2011.06.027.

Faidi, A., Stumbè, J.F., Safta, F., Sfar, S., 2022. Implementation of response surface methodology for the optimization of the extraction of sodium alginate from Padina pavonica brown algae. J. Food Meas. Char. 16, 4457–4469. https://doi.org/10.1007/s11694-022-01513-z.

Falletta, E., Longhi, M., Di Michele, A., Boffito, D.C., Bianchi, C.L., 2022. Floatable graphitic carbon nitride/alginate beads for the photodegradation of organic pollutants under solar light irradiation. J. Clean. Prod. 371, 133641 https://doi.org/10.1016/j.jclepro.2022.133641.

Falletta, E., Galloni, M.G., Mila, N., bin Roslan, M.N., Abd Ghani, N., Cerrato, G., Giordana, A., Magni, M., Spriano, S., Boffito, D.C., Bianchi, C.L., 2023. Fast and efficient piezo-photocatalytic mineralization of ibuprofen by BiOBr nanosheets under solar light irradiation. ACS Photonics 10 (11), 3929–3943. https://doi.org/10.1021/acsphotonics.3c00724, 2023.

Fan, H., Zhang, S., Ju, P., Su, H., Ai, S., 2012. Flower-like Bi$_2$Se$_3$ nanostructures: synthesis and their application for the direct electrochemistry of hemoglobin and H$_2$O$_2$ detection. Electrochim. Acta 64, 171–176. https://doi.org/10.1016/j.electacta.2012.01.010.

Feng, X., Guo, H., Patel, K., Zhou, H., Lou, X., 2014. High performance, recoverable Fe$_3$O$_4$ single bond ZnO nanoparticles for enhanced photocatalytic degradation of phenol. Chem. Eng. J. 244, 327–334. https://doi.org/10.1016/j.cej.2014.01.075.

Fuks, L., Filipiuk, D., Majdan, M., 2006. Transition metal complexes with alginate biosorbent. J. Mol. Struct. 792–793, 104–109. https://doi.org/10.1016/j.molstruc.2005.12.053.

Gao, X., Wang, Y., Peng, S., Yue, B., Fan, C., Chen, W., Li, X., 2015. Comparative toxicities of bismuth oxybromide and titanium dioxide exposure on human skin keratinocyte cells. Chemosphere 135, 83–93. https://doi.org/10.1016/j.chemosphere.2015.03.075.

Galloni, M.G., Ferrara, E., Falletta, E., Bianchi, C.L., 2022a. Olive mill wastewater remediation: from conventional approaches to photocatalytic processes by easily recoverable materials. Catalysts 12 (8), 923. https://doi.org/10.3390/catal12080923.

Galloni, M.G., Bortolotto, V., Falletta, E., Bianchi, C.L., 2022b. pH-driven selective adsorption of multi-dyes solutions by loofah sponge and polyaniline-modified loofah sponge. Polymers 14 (22), 4897. https://doi.org/10.3390/polym14224897.

Galloni, M.G., Cerrato, G., Giordana, G., Falletta, E., Bianchi, C.L., 2022c. Sustainable solar light photodegradation of diclofenac by nano- and micro-sized SrTiO₃. Catalysts 12 (8), 804. https://doi.org/10.3390/catal12080804.

Galloni, M.G., Falletta, E., Mahdi, M., Cerrato, G., Giordana, A., Boffito, D.C., Bianchi, C.L., 2024a. An innovative sunlight-driven device for photocatalytic drugs degradation: from laboratory- to real-scale application. A first step toward vulnerable communities. Advanced Sustainable Systems 2300565. https://doi.org/10.1002/adsu.202300565.

Galloni, M.G., Adeel Sharif, H.M., Grainca, A., Rizwan Haider, M., Djellabi, R., 2024b. Chapter 5: magnetic adsorbents/photocatalysts for water purification: progress and challenges in: novel materials and water purification: towards a sustainable future. https://doi.org/10.1039/9781837671663.

Gao, X., Xu, Z., Liu, G., Wu, J., 2021. Polyphenols as a versatile component in tissue engineering. Acta Biomater. 119, 57–74. https://doi.org/10.1016/j.actbio.2020.11.004.

Gao, X., Guo, C., Hao, Z., Zhao, Z., Long, H., Li, M., 2020. Adsorption of heavy metal ions by sodium alginate based adsorbent-a review and new perspectives. Int. J. Biol. Macromol. 164, 4423–4434. https://doi.org/10.1016/j.ijbiomac.2020.09.046.

Hamam, M., Chinnici, G., Di Vita, G., Pappalardo, G., Pecorino, B., Maesano, G., D'Amico, M., 2021. Circular economy models in agro-food systems: a review. Sustainability 13, 3453. https://doi.org/10.3390/su13063453.

Haque, F., Fan, C., Lee, Y.Y., 2023. From waste to value: addressing the relevance of waste recovery to agricultural sector in line with circular economy. J. Clean. Prod. 415, 137873 https://doi.org/10.1016/j.jclepro.2023.137873.

Hassaan, M.A., El- Nemr, M.A., Elkatory, M.R., Ragab, S., Niculescu, V.C., El- Nemr, A., 2023. Principles of photocatalysts and their different applications: a review. Top. Curr. Chem. 381, 31. https://doi.org/10.1007/s41061-023-00444-7.

Heydaripour, J., Gazi, M., Oladipo, A.A., Gulcan, H.O., 2019. A novel magnetic mesoporous resorcinol–melamine–formaldehyde resin for removal of phenols from aqueous solution. J. Porous Mater. 26, 1249–1258. https://doi.org/10.1007/s10934-018-0714-0.

Hernandez-Delgadillo, R., García-Cuéllar, C.M., Sánchez-Pérez, Y., Pineda-Aguilar, N., Martínez-Martínez, M.A., Rangel-Padilla, E.E., Nakagoshi-Cepeda, S.E., Solís-Soto, J. M., Sánchez-Nájera, R.I., Nakagoshi-Cepeda, M.A.A., Chellam, S., Cabral-Romero, C., 2018. In vitro evaluation of the antitumor effect of bismuth lipophilic nanoparticles (BisBAL NPs) on breast cancer cells. Int. J. Nanomed. 13, 6089–6097. https://doi.org/10.2147/IJN.S179095.

Hider, R.C., Liu, Z.D., Khodr, H.H., 2001. Metal chelation of polyphenols. Methods Enzymol. 335, 190–203. https://doi.org/10.1016/S0076-6879(01)35243-6.

Hu, Q., Sun, W., Tao, R., 2022. Rational construction of tetraphenylporphyrin/bismuth oxybromide nanocomposite with accelerated interfacial charge transfer for promoted visible-light-driven degradation of antibiotics. Res. Chem. Intermed. 48, 235–250. https://doi.org/10.1007/s11164-021-04620-6.

Hussain, A., Hou, J., Tahir, M., Ali, S.S., Rehman, Z.U., Bilal, M., Zhang, T., Dou, Q., Wang, X., 2022. Recent advances in BiOX-based photocatalysts to enhanced efficiency for energy and environment applications. Catalysis Review 66 (1), 119–173. https://doi.org/10.1080/01614940.2022.2041836.

Idris, A., Ismail, N.S.M., Hassan, N., Misran, E., Ngomsik, A.F., 2012. Synthesis of magnetic alginate beads based on maghemite nanoparticles for Pb (II) removal in aqueous solution. J. Ind. Eng. Chem. 18 (5), 1582–1589. https://doi.org/10.1016/j.jiec.2012.02.018.

Inglezakis, V.J., Moreno, J.L., Doula, M., 2012. Olive oil waste management EU legislation: current situation and policy recommendations. International Journal of Chemical and Environmental Engineering Systems 3 (2), 65–77. ISSN: 0976-3716.

Jamrah, A., Al-Zghoul, T.M., Darwish, M.M., 2023. A comprehensive review of combined processes for olive mill wastewater treatments. Case Studies in Chemical and Environmental Engineering 8, 100493. https://doi.org/10.1016/j.cscee.2023.100493.

Lai, Y.L., Thirumavalavan, M., Lee, J.F., 2009. Effective adsorption of heavy metal ions (Cu²⁺, Pb²⁺, Zn²⁺) from aqueous solution by immobilization of adsorbents on Ca-alginate beads. Toxicol. Environ. Chem. 92 (4), 697–705. https://doi.org/10.1080/02772240903057382.

Lendzion-Bielun, Z., Wojciechowska, A., Grzechulska-Damszel, J., Narkiewicz, U., Sniadecki, Z., Idzikowski, B., 2020. Effective processes of phenol degradation on Fe₃O₄–TiO₂ nanostructured magnetic photocatalyst. J. Phys. Chem. Solid. 136, 109178 https://doi.org/10.1016/j.jpcs.2019.109178.

Li, B., Dong, Y., Zou, C., Xu, Y., 2014. Iron (III)–alginate fiber complex as a highly effective and stable heterogeneous fenton photocatalyst for mineralization of organic dye. Ind. Eng. Chem. Res. 53 (11), 4199–4206. https://doi.org/10.1021/ie404241r.

Li, C., Zheng, Y., Wang, X., Feng, S., Di, D., 2011. Simultaneous separation and purification of flavonoids and oleuropein from Olea europaea L. (olive) leaves using macroporous resin. J. Sci. Food Agric. 91, 2826–2834. https://doi.org/10.1002/jsfa.4528.

Li, W., Fan, Y., Lin, J., Yu, P., Wang, Z., Ning, C., 2022. Near-infrared light-activatable bismuth-based nanomaterials for antibacterial and antitumor treatment. Advanced Theurapetics 5 (9), 2200027. https://doi.org/10.1002/adtp.202200027.

Li, Y., Du, Q., Liu, T., Wang, Y., Wu, S., Wang, Z., Xia, Y., Xia, L., 2013. Methylene blue adsorption on graphene oxide/calcium alginate composites. Carbohydrate Polymers 95 (1), 501–507. https://doi.org/10.1016/j.carbpol.2013.01.094.

Li, X., Wang, L., Zhang, L., Zhuo, S., 2017. A facile route to the synthesis of magnetically separable BiOBr/NiFe₂O₄ composites with enhanced photocatalytic performance. Appl. Surf. Sci. 419, 586–594. https://doi.org/10.1016/j.apsusc.2017.05.013.

Li, X., Xu, H., Wang, L., Zhang, L., Cao, X., Guo, Y., 2018. Spinel NiFe₂O₄ nanoparticles decorated BiOBr nanosheets for improving the photocatalytic degradation of organic dye pollutants. J. Taiwan Inst. Chem. Eng. 85, 257–264. https://doi.org/10.1016/j.jtice.2018.01.043.

Li, Z., Yin, Z., Xiao, W., Chen, Y., Yang, C., Luo, Y., Hong, Z., Xue, M., 2024. Facile construction of robust superhydrophobic ZIF-8@pulp/cellulose nanofiber (CNF) membrane for multifunctional applications. Ind. Crop. Prod. 209, 118001 https://doi.org/10.1016/j.indcrop.2023.118001.

Liu, J., Shi, J., Deng, H., 2023. Current status of research on BiOX-based heterojunction photocatalytic systems: synthesis methods, photocatalytic applications and prospects. J. Environ. Chem. Eng. 11 (5), 110311 https://doi.org/10.1016/j.jece.2023.110311.

Liu, Z., Wu, B., Zhao, Y., Niu, J., Zhu, Y., 2014. Solvothermal synthesis and photocatalytic activity of Al-doped BiOBr microspheres. Ceram. Int. 40 (4), 5597–5603. https://doi.org/10.1016/j.ceramint.2013.10.152.

Luo, Y., Han, Y., Xue, M., Xie, Y., Yin, Z., Xie, C., Li, X., Zheng, Y., Huang, J., Zhang, Y., Yang, Y., Gao, B., 2022. Ball-milled bismuth oxybromide/biochar composites with enhanced removal of reactive red owing to the synergy between adsorption and photodegradation. J. Environ. Manag. 308, 114652 https://doi.org/10.1016/j.jenvman.2022.114652.

Ma, M., Yang, Y., Chen, Y., Jiang, J., Ma, Y., Wang, Z., Huang, W., Wang, S., Liu, M., Ma, D., 2021a. Fabrication of hollow flowerlike magnetic Fe₃O₄/C/MnO₂/C₃N₄ composite with enhanced photocatalytic activity. Sci. Rep. 11, 2597. https://doi.org/10.1038/s41598-021-81974-2.

Ma, M., Yang, Y., Chen, Y., Ma, Y., Lyu, P., Cui, A., Huang, W., Zhang, Z., Li, Y., Si, F., 2021b. Photocatalytic degradation of MB dye by the magnetically separable 3D flower- like Fe₃O₄/SiO₂/MnO₂/BiOBr-Bi photocatalyst. J. Alloys Compd. 861, 158256 https://doi.org/10.3390/polym14224897.

Malik, M., Len, T., Luque, R., Osman, S.M., Paone, E., Khan, M.I., Wattoo, M.A., Jamshaid, M., Anum, A., Rehman, A., 2023. Investigation on synthesis of ternary g-C₃N₄/ZnO–W/M nanocomposites integrated heterojunction II as efficient photocatalyst for environmental applications. Environ. Res. 217, 114621 https://doi.org/10.1016/j.envres.2022.114621.

Mandal, B.B., Kundu, S.C., 2009. Calcium alginate beads embedded in silk fibroin as 3D dual drug releasing scaffolds. Biomaterials 30 (28), 5170–5177. https://doi.org/10.1016/j.biomaterials.2009.05.072.

Melchionna, M., Fornasiero, P., 2020. Updates on the roadmap for photocatalysis. ACS Catal. 10 (10), 5493–5501. https://doi.org/10.1021/acscatal.0c01204.

Melchiors, E., Bentes Freire, F., 2023. Winery wastewater treatment: a systematic review of traditional and emerging technologies and their efficiencies. Environmental Processes 10 (43). https://doi.org/10.1007/s40710-023-00657-4.

Meroni, D., Galloni, M.G., Cionti, C., Cerrato, G., Falletta, E., Bianchi, C.L., 2023. Efficient day-and-night NO₂ abatement by polyaniline/TiO₂ nanocomposites. Materials 16 (3), 1304. https://doi.org/10.3390/ma16031304.

Mishra, V., Baranwal, V., Mishra, R.K., Sharma, S., Paul, B., Pandey, A.C., 2017. Immunotoxicological impact and biodistribution assessment of bismuth selenide (Bi2Se3) nanoparticles following intratracheal instillation in mice. Sci. Rep. 7, 18032 https://doi.org/10.1038/s41598-017-18126-y.

Mustafa, F.S., Oladipo, A.A., Gazi, M., 2022. Photocatalytic degradation of toxic phenolic compound and bacterial inactivation by ternary Li doped Zn₀.₅Ni₀.₅Fe₂O₄. ChemistrySelect 7 (21), e202200727. https://doi.org/10.1002/slct.202200727.

Mustafa, F.S., Oladipo, A.A., 2023. Dual function Mg-doped binary metal ferrite: photocatalytic degradation of trichlorophenol, bactericidal activity and molecular docking analysis. Chemosphere 312, 137348. https://doi.org/10.1016/j.chemosphere.2022.137348.

Ndwabu, S., Malungana, M., Mahlambi, P., 2023. Phenolic compounds—occurrence in water, sediment and sludge, and ecological risk evaluation. Clean: Soil, Air, Water 51, 2200404. https://doi.org/10.1002/clen.202200404.

Nithya, M., Praveen, K., Sathya Balasubramanian, U.N., Pandurangan, A., 2018. Green synthesis of α-Fe₂O₃/BiPO₄ composite and its biopolymeric beads for enhanced photocatalytic application. J. Mater. Sci. Mater. Electron. 29 (17), 14733–14745. https://doi.org/10.1007/s10854-018-9610-2.

Nikazar, M., Alizadeh, M., Lalavi, R., Rostami, M.H., 2014. The optimum conditions for synthesis of Fe₃O₄/ZnO core/shell magnetic nanoparticles for photodegradation of phenol. J Environ Health Sci Engineer 12, 21. https://doi.org/10.1186/2052-336X-12-21.

Ou, Q., Zhang, S., Fu, C., Yu, L., Xin, P., Gu, Z., Cao, Z., Wu, J., Wang, Y., 2021. More natural more better: triple natural anti-oxidant puerarin/ferulic acid/polydopamine incorporated hydrogel for wound healing. J. Nanobiotechnol. 19, 237. https://doi.org/10.1186/s12951-021-00973-7.

Pan, Y., Zhang, Y., Hou, M., Xue, J., Qin, R., Zhou, M., Zhang, Y., 2023. Properties of polyphenols and polyphenol-containing wastewaters and their treatment by Fenton/Fenton-like reactions. Sep. Purif. Technol. 317, 123905 https://doi.org/10.1016/j.seppur.2023.123905.

Papageorgiou, S.K., Kouvelos, E.P., Favvas, E.P., Sapalidis, A.A., Romanos, G.E., Katsaros, F.K., 2010. Metal–carboxylate interactions in metal–alginate complexes

studied with FTIR spectroscopy. Carbohydr. Res. 345, 469–473. https://doi.org/10.1016/j.carres.2009.12.010.

Peramune, D., Manatunga, D.C., Dassanayake, R.S., Premalal, V., Liyanage, R.N., Gunathilake, C., Abidi, N., 2022. Recent advances in biopolymer-based advanced oxidation processes for dye removal applications: a review. Environ. Res. 215, 114242 https://doi.org/10.1016/j.envres.2022.114242.

Perez-Larran, P., Diaz-Reinoso, B., Moure, A., Alonso, J.L., Dominguez, H., 2018. Adsorption technologies to recover and concentrate food polyphenols. Curr. Opin. Food Sci. 23, 165–172. https://doi.org/10.1016/j.cofs.2017.10.005.

Pozzo, R.L., Baltanás, M.A., Cassano, A.E., 1997. Supported titanium oxide as photocatalyst in water decontamination: state of the art. Catal. Today 39, 219–231. https://doi.org/10.1016/S0920-5861(97)00103-X.

Rengifo-Herrera, J.A., Pulgarin, C., 2023. Why five decades of massive research on heterogeneous photocatalysis, especially on TiO$_2$, has not yet driven to water disinfection and detoxification applications? Critical review of drawbacks and challenges. Chem. Eng. J. 477, 146875 https://doi.org/10.1016/j.cej.2023.146875.

Riccucci, G., Cazzola, M., Ferraris, S., Gobbo, V.A., Guaita, M., Spriano, S., 2021a. Surface functionalization of Ti$_6$Al$_4$V with an extract of polyphenols from red grape pomace. Mater. Des. 206, 109776 https://doi.org/10.1016/j.matdes.2021.109776.

Riccucci, G., Cazzola, M., Ferraris, S., Gobbo, V.A., Miola, M., Bosso, A., Orlygsson, G., Ng, C.H., Vernè, E., Spriano, S., 2021b. Surface functionalization of bioactive glasses and hydroxyapatite with polyphenols from organic red grape pomace. J. Am. Ceram. Soc. 105, 1697–1710. https://doi.org/10.1111/jace.17849.

Riccucci, G., Ferraris, S., Reggio, C., Bosso, A., Orlygsson, G., Ng, C.H., Spriano, S., 2021c. Polyphenols from grape pomace: functionalization of chitosan-coated hydroxyapatite for modulated swelling and release of polyphenols. Langmuir 37 (51), 14793–14804. https://doi.org/10.1021/acs.langmuir.1c01930.

Rocher, V., Siaugue, J.M., Cabull, V., Bee, A., 2008. Removal of organic dyes by magnetic alginate beads. Water Res. 42 (4–5), 1290–1298. https://doi.org/10.1016/j.watres.2007.09.024.

Saleh, Z.S., Wibisono, R., Lober, K., 2008. Recovery of polyphenolics from apple juice utilizing adsorbent polymer technology. Int. J. Food Eng. https://doi.org/10.2202/1556-3758.1383.

Salem, N.M., Ahmad, A.L., Awwad, A.M., 2013. New route for synthesis magnetite nanoparticles from ferrous ions and pistachio leaf extract. Nanosci. Nanotechnol. 3 (3), 48–51. https://doi.org/10.5923/j.nn.20130303.03.

Sakthivel, S., Neppolian, B., Shankar, M.V., Arabindoo, B., Palanichamy, A., Murugesan, V., 2003. Solar photocatalytic degradation of azo dye: comparison of photocatalytic efficiency of ZnO and TiO$_2$. Sol. Energy Mater. Sol. Cells 77, 65–82. https://doi.org/10.1016/S0927-0248(02)00255-6.

Shahbazi, M.A., Faghfouri, L., Ferreira, M.P.A., Figueiredo, P., Maleki, H., Sefat, F., Hirvonen, J., Santos, H.A., 2020. The versatile biomedical applications of bismuth-based nanoparticles and composites: therapeutic, diagnostic, biosensing, and regenerative properties. Chem. Soc. Rev. 49, 1253–1321. https://doi.org/10.1039/C9CS00283A.

Sharma, K., Dutta, V., Sharma, S., Raizada, P., Hosseini- Bandegharaei, A., Thakur, P., Singh, P., 2019. Recent advances in enhanced photocatalytic activity of bismuth oxyhalides for efficient photocatalysis of organic pollutants in water: a review. J. Ind. Eng. Chem. 78, 1–20. https://doi.org/10.1016/j.jiec.2019.06.022.

Somo, S.I., Khanna, O., Brey, E.M., 2017. Alginate microbeads for cell and protein delivery. Cell Microencapsulation. Humana Press, New York, pp. 217–224. https://doi.org/10.1007/978-1-4939-6364-5_17.

Springmann, M., Clark, M., Mason-D'Croz, D., Wiebe, K., Bodirsky, B.L., Lassaletta, L., de Vries, W., Vermeulen, S.J., Herrero, M., Carlson, K.M., Jonell, M., Troell, M., DeClerck, F., Gordon, L.J., Zurayk, R., Scarborough, P., Rayner, M., Loken, B., Fanzo, J., Godfray, H.C.J., Tilman, D., Rockström, J., Willett, W., 2018. Options for keeping the food system within environmental limits. Nature 562, 519–525. https://doi.org/10.1038/s41586-018-0594-0.

Stewart, C., Konstantinov, K., McKinnon, S., Guatelli, S., Lerch, M., Rosenfeld, A., Tehei, M., Corde, S., 2016. First proof of bismuth oxide nanoparticles as efficient radiosensitisers on highly radioresistant cancer cells. Phys. Med. 32 (11), 1444–1452. https://doi.org/10.1016/j.ejmp.2016.10.015.

Thamarai, P., Kamalesh, R., Saravanan, A., Swaminaathan, P., Deivaynai, V.C., 2024. Emerging trends and promising prospects in nanotechnology for improved remediation of wastewater contaminants: present and future outlooks. Environ. Nanotechnol. Monit. Manag. 21, 100913 https://doi.org/10.1016/j.enmm.2024.100913.

THE 17 GOALS. https://sdgs.un.org/goals.

Tosti, S., Accetta, C., Fabbricino, M., Sansovini, M., Pontoni, L., 2013. Reforming of olive mill wastewater through a Pd-membrane reactor. Int. J. Hydrogen Energy 38 (25), 10252–10259. https://doi.org/10.1016/j.ijhydene.2013.06.027.

Vaiano, V., Matarangolo, M., Murcia, J.J., Rojas, H., Navio, J.A., Hidalgo, M.C., 2018. Enhanced photocatalytic removal of phenol from aqueous solutions using ZnO modified with Ag. Appl. Catal. B Environ. 225, 197–206. https://doi.org/10.1016/j.apcatb.2017.11.075.

Vinoth, S., Ong, W.-J., Pandikumar, A., 2022. Defect engineering of BiOX (X = Cl, Br, I) based photocatalysts for energy and environmental applications: current progress and future perspectives. Coord. Chem. Rev. 464, 214541 https://doi.org/10.1016/j.ccr.2022.214541.

Wang, R., Li, H., Sun, H., 2019a. Bismuth: environmental pollution and health effects. Encyclopedia of Environmental Health 415–423. https://doi.org/10.1016/B978-0-12-409548-9.11870-6.

Wang, Z., Chen, M., Huang, D., Zeng, G., Xu, P., Zhou, C., Lai, C., Wang, H., Cheng, M., Wang, W., 2019b. Multiply structural optimized strategies for bismuth oxyhalide photocatalysis and their environmental application. Chem. Eng. J. 374, 1025–1045. https://doi.org/10.1016/j.cej.2019.06.018.

Watson, M., 2020. Waste management. In: Kobayashi, A. (Ed.), International Encyclopedia of Human Geography, second ed. Elsevier, Oxford, pp. 225–231. https://doi.org/10.1016/B978-0-08-102295-5.10761-9.

Won, K., Kim, S., Kim, K.J., Park, H.W., Moon, S.J., 2005. Optimization of lipase entrapment in Ca-alginate gel beads. Process Biochem. 40 (6), 2149–2154. https://doi.org/10.1016/j.procbio.2004.08.014.

Yin, Z., Li, Z., Deng, Y., Xue, M., Chen, Y., Ou, J., Xie, Y., Luo, Y., Xie, C., Hong, Z., 2023. Multifunctional CeO2-coated pulp/cellulose nanofibers (CNFs) membrane for wastewater treatment: effective oil/water separation, organic contaminants photodegradation, and anti-bioadhesion activity. Ind. Crop. Prod. 197, 116672 https://doi.org/10.1016/j.indcrop.2023.116672.

Zhao, Y., Guo, H., Xia, Q., Liu, J., Liang, X., Liu, E., Fan, J., 2022. Effective photodegradation of rhodamine B and levofloxacin over CQDs modified BiOCl and BiOBr composite: mechanism and toxicity assessment. J. Colloid Interface Sci. 627, 180–193. https://doi.org/10.1016/j.jcis.2022.07.046.

Zhou, C., Liang, Y., Xia, W., Almatrafi, E., Song, B., Wang, Z., Zeng, Y., Yang, Y., Shang, Y., Wang, C., Zeng, G., 2023. Single atom Mn anchored on N-doped porous carbon derived from spirulina for catalyzed peroxymonosulfate to degradation of emerging organic pollutants. J. Hazard Mater. 441, 129871 https://doi.org/10.1016/j.jhazmat.2022.129871.

Zhou, R., Wang, H., Yang, Y., Zhang, C., Dong, X., Du, J., Yan, L., Zhang, G., Gu, Z., Zhao, Y., 2019. Tumor microenvironment-manipulated radiocatalytic sensitizer based on bismuth heteropolytungstate for radiotherapy enhancement. Biomaterials 189, 11–22. https://doi.org/10.1016/j.biomaterials.2018.10.016.

Zhu, Z., Lu, Z., Wang, D., Tang, X., Yan, Y., Shi, W., Wang, Y., Gao, N., Yao, X., Shi, W., Wang, Y., Gao, N., Yao, X., Dong, H., 2016. Construction of high-dispersed Ag/Fe$_3$O$_4$/g-C$_3$N$_4$ photocatalyst by selective photo-deposition and improved photocatalytic activity. Appl. Catal. B Environ. 182, 115–122. https://doi.org/10.1016/j.apcatb.2015.09.029.